Graz University of Technology

Adrian Ruckhofer, BSc

Surface dynamics of the topological insulator Bi_2Se_3 from helium atom scattering

MASTER'S THESIS

to achieve the university degree of
Diplom-Ingenieur

Masterstudium Technische Physik

Graz University of Technology
Institute of Experimental Physics

Supervisor:
Univ.-Prof. Mag. Dr.rer.nat Wolfgang E. Ernst
Institute of Experimental Physics

Co-advisor:
Dipl.-Ing. Dr.techn. Anton Tamtögl
Institute of Experimental Physics

Graz, Mai 2017

Deutsche Fassung:
Beschluss der Curricula-Kommission für Bachelor-, Master- und Diplomstudien vom 10.11.2008
Genehmigung des Senates am 1.12.2008

EIDESSTATTLICHE ERKLÄRUNG

Ich erkläre an Eides statt, dass ich die vorliegende Arbeit selbstständig verfasst, andere als die angegebenen Quellen/Hilfsmittel nicht benutzt, und die den benutzten Quellen wörtlich und inhaltlich entnommenen Stellen als solche kenntlich gemacht habe.

Graz, am ……. ……..
(Unterschrift)

Englische Fassung:

STATUTORY DECLARATION

I declare that I have authored this thesis independently, that I have not used other than the declared sources / resources, and that I have explicitly marked all material which has been quoted either literally or by content from the used sources.

……. ……..
date (signature)

Abstract

This work presents an experimental study of the surface vibrational modes of the topological insulator Bi_2Se_3. Topological insulators are insulating in the bulk but exhibit conducting surface states. Applications include nonlinear optics and thermoelectricity as well as possible future applications in spintronics replacing conventional electronics. This unique class of materials has received great attention, however, very limited experimental data exist for the surface phonon dispersion of $Bi_2Se_3(111)$ as well as for the region of acoustic phonon modes on topological insulator surfaces in general.

Using inelastic helium atom scattering the surface phonon modes of $Bi_2Se_3(111)$ have been studied. Using various scattering conditions the surface phonon dispersion of Bi_2Se_3 was extracted for the entire Brillouin zone. Measurements at a surface temperature of 123 K and at room temperature were carried out along both high symmetry crystal directions. Phonons with energies up to 18 meV have been detected.

The low energy region of the lattice vibrations is mainly dominated by the strong Rayleigh mode which has been claimed to be absent in previous experimental studies. In contradiction to previous works no Kohn-Anomaly is observed. Using the slope of the Rayleigh mode close to the Brillouin zone centre the group velocity of the phonons at the surface were determined to be $v_g = (1560 \pm 44)\,\mathrm{m\,s^{-1}}$.

Simulations based on density functional perturbation theory are in good agreement with the experimental data.

In addition to the surface phonon dispersion the surface Debye temperature is determined and the Debye-Waller factor calculated using elastic helium atom scattering. The thermal attenuation of the elastic diffraction peak lead to a surface Debye temperature of $(114 \pm 6)\,\mathrm{K}$.

Apparative extensions to the apparatus included the addition of a load lock chamber, which was added to the whole setup. The newly designed chamber with its mounting rack allows easier access to the main chamber. Sample changes can now be performed without venting of the main chamber using a sample transfer system. In addition the sample surface can be prepared *in situ* and surface contamination can be held at a minimum.

Kurzfassung

Diese Arbeit präsentiert eine experimentelle Untersuchung der Vibrationsmoden des topologischen Isolators Bi_2Se_3. Topologische Isolatoren sind im Inneren des Materials Isolatoren, aber besitzen leitende Zustände an der Oberfläche. Diese Materialien finden Anwendung in nichtlinearer Optik und Thermoelektrizität. Mögliche Anwendungen in der Zukunft gibt es im Feld Spintronik zur Ersetzung von herkömmlicher Elektronik. Diese einzigartigen Materialien haben in den letzten Jahren immer mehr an Bedeutung gewonnen, jedoch sind über die Oberflächenphononen dieser Materialien nur sehr wenig experimentelle Daten vorhanden.
Die Dispersion der Oberflächenphononen von Bi_2Se_3 wurde unter Verwendung von Helium Atom Streuung untersucht. Mit Hilfe von Streuexperimenten unter verschiedensten Bedingungen wurde die Oberflächenphononen Dispersion für die gesamte Brillouin Zone bestimmt. Sowohl Messungen mit einer Probentemperatur von 123 K also auch bei Raumtemperatur wurden entlang der beiden Hochsymmetrierichtungen des Kristalls aufgenommen. Phononen mit Energien bis zu 18 meV konnten gemessen werden.
Der niedrige Energiebereich der Dispersion wird von einem starken Rayleigh Mode dominiert, der in vorherigen Untersuchungen nicht aufscheint. Im Widerspruch zu früheren Arbeiten konnte keine Kohn-Anomaly festgestellt werden. Aus der Steigung der Rayleigh Mode konnte die Gruppengeschwindigkeit der Phononen auf der Oberfläche mit $v_g = (1560 \pm 44)\,\mathrm{m\,s^{-1}}$ bestimmt werden.
Theoretische Simulationen unter der Verwendung von störungstheoretischer Dichte Funktional Theorie stimmen gut mit den vorhandenen Messungen überein.
Zusätzlich zur Oberflächenphononen Dispersion wurde die Oberflächen Debye-Temperatur bestimmt und der Debye-Waller Faktor berechnet. Aus der thermischen Abschwächung des elastischen Peaks nullter Ordnung ergab sich eine Debye-Temperatur von (114 ± 6) K.
Am experimentellen Aufbau in Graz wurde zusätzlich eine Schleusenkammer montiert. Die speziell entwickelte Kammer ermöglicht einen erleichterten Zugang zur Hauptkammer. Der Probentransfer kann nun durchgeführt werden ohne die ganze Hauptkammer zu belüften. Zusätzlich kann die Probenpräparation *in situ* erfolgen, um die Verunreinigungen der Probe zu verhindern.

Contents

List of Figures

1 Introduction

Within the last decades two-dimensional materials and materials with special surface restricted properties got more and more attention. One of these materials is the class of topological insulators. To investigate these types of materials measurements that are truly surface specific are important. In such measurements the influence of bulk values has to be at a minimum. One of these measurement methods is helium atom scattering (HAS). HAS is perfectly suited to study surface specific properties. Other probe particles for scattering like neutrons or electrons penetrate the surface at a minimum of a few atomic layers. On the other hand low-energetic helium atoms interact with the electron density 2-3 Å above the first atomic layer. HAS is thus dependent on the electron density variations of the material surface and completely surface sensitive. Another important property of HAS is the non destructive way of interaction. Depending on the kinetic energy of other scattering particles methods the sample can be slightly damaged. The surface sensitivity and soft surface treatment of HAS can be attributed to the electrical and magnetical inertness of the helium atom.
Within the whole field of physics surface properties are of great importance. All interactions and reactions between materials take place at material surfaces. Those include chemical reactions using a catalyst and processes such as friction and corrosion. In such processes the accurate structure and the interaction between the surface of the sample and the incoming interacting particles play an important role.
Even though the analysis poses a certain challenge to the experimental setup, the surfaces of topological insulators such as Bi_2Se_3 have received more interest over the last years. In addition to their fundamental interest, these materials are useful for applications ranging from spintronics to quantum computation. Spintronics uses the intrinsic spin of the electron and its magnetic moment in solid-state devices. The electronic structure of topological insulators has been widely studied using Angle-resolved photoemission spectroscopy (ARPES). However, very limited information about the surface lattice dynamics is available up to now. In particular the acoustic surface phonon modes of these materials are in a low energy region which can only be measured using HAS.
Nevertheless an exact knowledge of the surface phonon dispersion is important to understand the thermoelectric properties of Bi_2Se_3. Moreover, scattering of electrons by phonons via the electron-phonon interaction may impose constraints to surface-dominated transport in technological applications.

In this work first the experimental setup, where all the measurements were taken is explained. Afterwards the theoretical background is given with a more detailed part about topological insulators. All measurements and important results are covered in the main part of this work.

2 Experimental Setup

All measurements of this work have been recorded on the helium atom scattering apparatus called H.A.N.S (Helium Atom Nondestructive Scattering). The whole apparatus was originally designed and built at the FU Berlin and then transferred to Graz, where the system was rebuilt and characterized.[1,2]. During the first work several adaptions and improvements[3] were done. The first measurements were done with Bi(111)[2,4–7] and Sb(111)[3,8–11]. The static and dynamic behavior of the surface of these materials was investigated.
In the following the most important parameters and features of the apparatus will be described. A much more sophisticated description of the apparatus including the whole construction, beam geometry and vacuum setup is treated in the PhD thesis of Anton Tamtögl[2].
The goal of the whole apparatus is to generate a monochromatic helium beam which then hits a surface and is detected in the end. Due to the wave-particle duality (de Broglie) a characteristic wavelength λ can be assigned to the helium beam. Interference pattern occur when the helium beam hits the surface. From the interference pattern information about the surface structure and lattice constants can be given.

2.1 Source Arm

The source arm (see fig. 2.1) consists of 2 chambers which host all the necessary equipment to produce the nearly monoenergetic atomic beam. The helium gas is expanded through a narrow nozzle of diameter d (around 10 µm) into the vacuum chamber which is held at a low pressure of $p_a \leqslant 10^{-7}$ mbar. Due to the high pressure difference of 9 orders of magnitude between the in- and the outside of the nozzle, the gas undergoes a supersonic expansion. This expansion happens so fast that the whole process may be assumed to be adiabatic. Therefore the thermal energy of the particle is transformed into translational energy[12,13].
The central part of this helium beam is selected by a so called 'skimmer'. This conical-shaped aperture is located between the first and the second chamber. The remaining beam is mainly characterized by a very narrow velocity distribution width of around

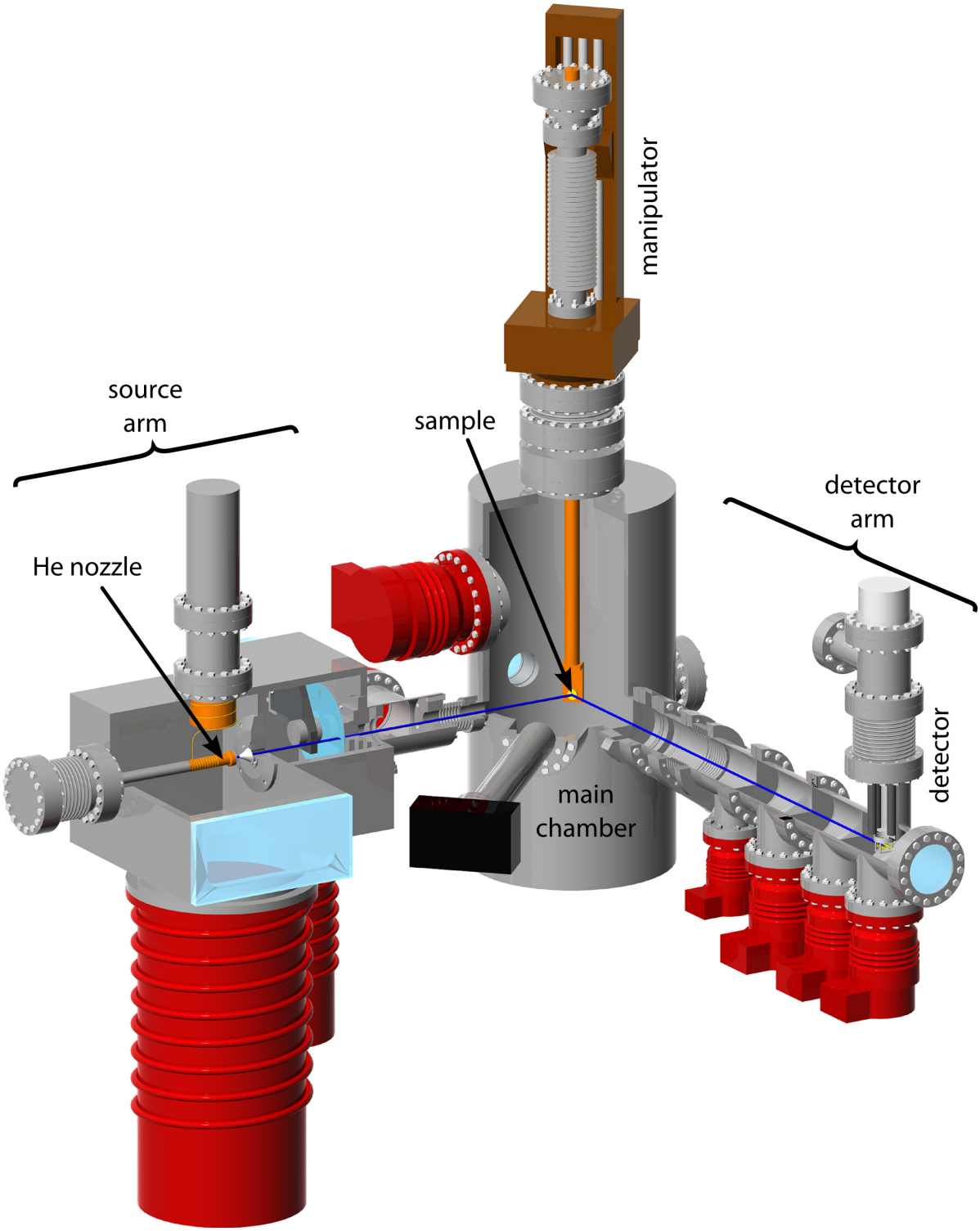

Figure 2.1: Basic representation of the apparatus used for all measurements. Image taken from A. Tamtögl[2]

$\Delta v_{\parallel}/v_{\parallel} \simeq 1\%$. The final particle velocity of the beam is given by

$$v_{\parallel} = \sqrt{\frac{5k_{\mathrm{B}}T_0}{m_{He}}}, \tag{2.1}$$

with k_{B} being the Boltzmann's constant and m_{He} the atomic mass of helium. All important atomic scattering process parameters depend on this velocity.
Another important scattering parameter is the absolute value of the particle wavevector $\mathbf{k}_i$:

$$\mathbf{k}_i^2 = \frac{2m_{He}}{\hbar^2}E_i \tag{2.2}$$

with E_i being the beam energy:

$$E_i = \frac{5}{2}k_{\mathrm{B}}T_0 \tag{2.3}$$

These values will play an important role in the analysis of the measured data. The beam energy and thus the wave vector can be easily adjusted by changing the temperature of the nozzle T_0. The apparatus in Graz can be adjusted to stable nozzle temperatures between 48 K and 170 K, resulting in scattering energies between 10 meV and 37 meV.
After the central part of the beam has been filtered out with the skimmer, the beam enters the next chamber of the source arm. This chamber contains a rotating chopper disc. This is one of the important parts to be able to perform time-of-flight (TOF) measurements. As the name suggests the travel time of the particles between arriving at the detector and the chopper disc is identified. In a normal scattering scenario the continuous beam is scattered from the sample and the helium atoms arriving at the detector are integrated over time. For TOF measurements one needs to distinguish between the particle velocities. Therefore the incoming particle beam is 'chopped' into discrete packets using the thin slits on the rotating chopper disc. After the beam went through the second chamber it enters the main chamber through an aperture. The main chamber can be separated from the source arm with a valve when no measurements are performed.

2.2 Main Chamber

In the main chamber (MC) the sample is located on a seven-axis manipulator. With this manipulator the sample can be moved to the desired scattering position. By adjustment of the z-direction the sample can also be moved to the position of the low energy electron diffraction (LEED) system. During all measurements the main chamber is constantly kept at ultra high vacuum (UHV) conditions (p = 10^{-10} - 10^{-11} mbar) using turbo molecular pumps. This prevents the surface of the sample from getting contaminated by adsorption of gas molecules over the time-scale of the experiment. To monitor the residual gases in the MC a quadrupole mass spectrometer is located in the MC. To clean

the surface of the samples by annealing a button heater is attached to the backside of the sample holder. To heat the manipulator itself a Thermocoax heating wire is used. The same heating wire is also connected to a liquid nitrogen reservoir which can be used to cool the sample to temperatures of about 100 K. For alignment of the crystal rotation in the high symmetry orientation a LEED is used. To monitor the cleanliness of the surface the LEED is combined with an AES (Auger electron spectroscopy) using a retarding field detector built into the LEED screen.

2.3 Detector Arm

The detector arm setup is flanged onto the main chamber at a total angle of 91.5° with respect to the source arm. In this setup the position of both arms stays always fixed. The detector arm mainly consists of a differentially pumped separation stage, which the helium atoms have to traverse to arrive at the quadrupol mass spectrometer for detection. After inelastic interaction with the surface, the helium atoms have gained or lost energy ($\Delta E \neq 0$), resulting in a different total speed in comparison to the elastically scattered beam. The separation distance enables these energetic differences to spread the different helium atoms spatially. Due to this separation, the atoms arrive at the detector at different times and can be distinguished.

2.4 Addition of a load lock chamber

During this work a new arm was flanged onto the MC. This addition to the apparatus now allows for faster sample changes as well as easier access into the MC for smaller repairs. Previous to this adjustment the whole manipulator had to be unscrewed and taken out of the top in order to put a new sample into the sample holder. This time consuming procedure was then followed by baking the whole MC for a few days until the desired pressure condition was reached. Due to residual H_2O in the MC the baking process has to last for such a long time.
To improve the changing of samples the new load-lock chamber (LLC) was designed and built. Therefore a T-shaped chamber was mounted directly to the MC. A Turbo molecular pump can be screwed onto the bottom flange of this chamber. At the top a fast entry door with a see-through window is placed which can be opened. Onto the remaining part of the chamber a sample transfer system can be flanged. Such a system consists of a magnetically coupled arm with a gripper at the front. The whole transfer system is kept at ultra high vaccum by an ion pump and a Non-Evaporable Getter (NEG) pump. To achieve the necessary fore-vacuum for the TMP a small plateau is located under the

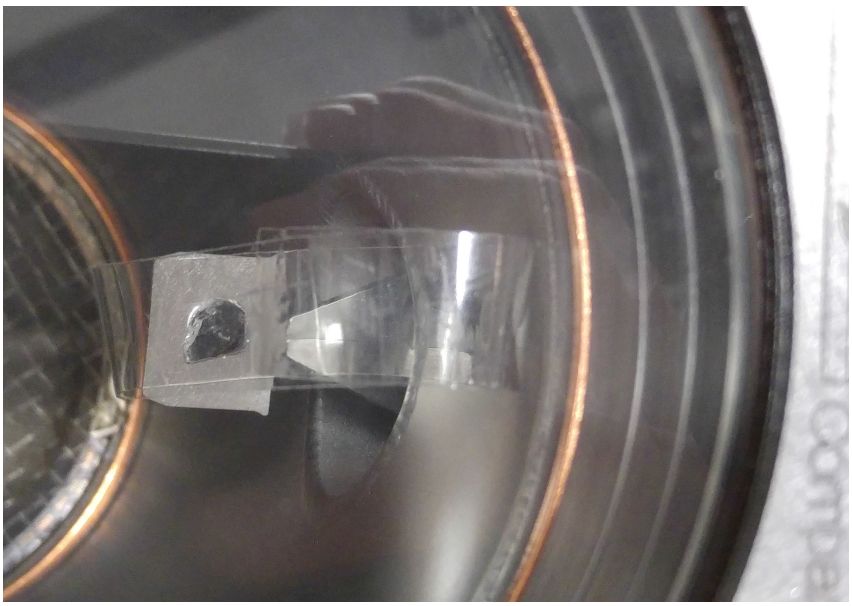

Figure 2.2: Picture of the *in-situ* sample preparation using a scotch tape which is fixated at the surface of the sample and the chamber wall. By moving the gripper with the sample mount to the left the uppermost layer gets peeled off. Contamination is avoided by performing the whole process under UHV conditions.

transfer system to host a rotary vane pump. In figure 2.3 the whole system holding the LLC is shown.

The procedure of putting a new sample into the sample holder in the MC now becomes much easier. First, one has to open the top window (TMP, rotary vane pump and ion pump are switched off) and put the sample mount into the gripper. For sample preparation we used the convenient method of ripping the uppermost layers off with a scotch tape. Therefore the scotch tape is pasted onto the sample and on the chamber wall. After closing the window and evacuating the whole system the uppermost layers can be ripped off by simply moving the long arm into the MC. This *in-situ* method of sample preparation under UHV conditions is essential to avoid contamination of the surface. In figure 2.2 the sample prepared with the scotch tape in the LLC can be seen.
With a bit of precision work the sample holder can be put into the manipulator. After the arm left the MC and the valve is closed the whole transfer system and the LLC can be vented.

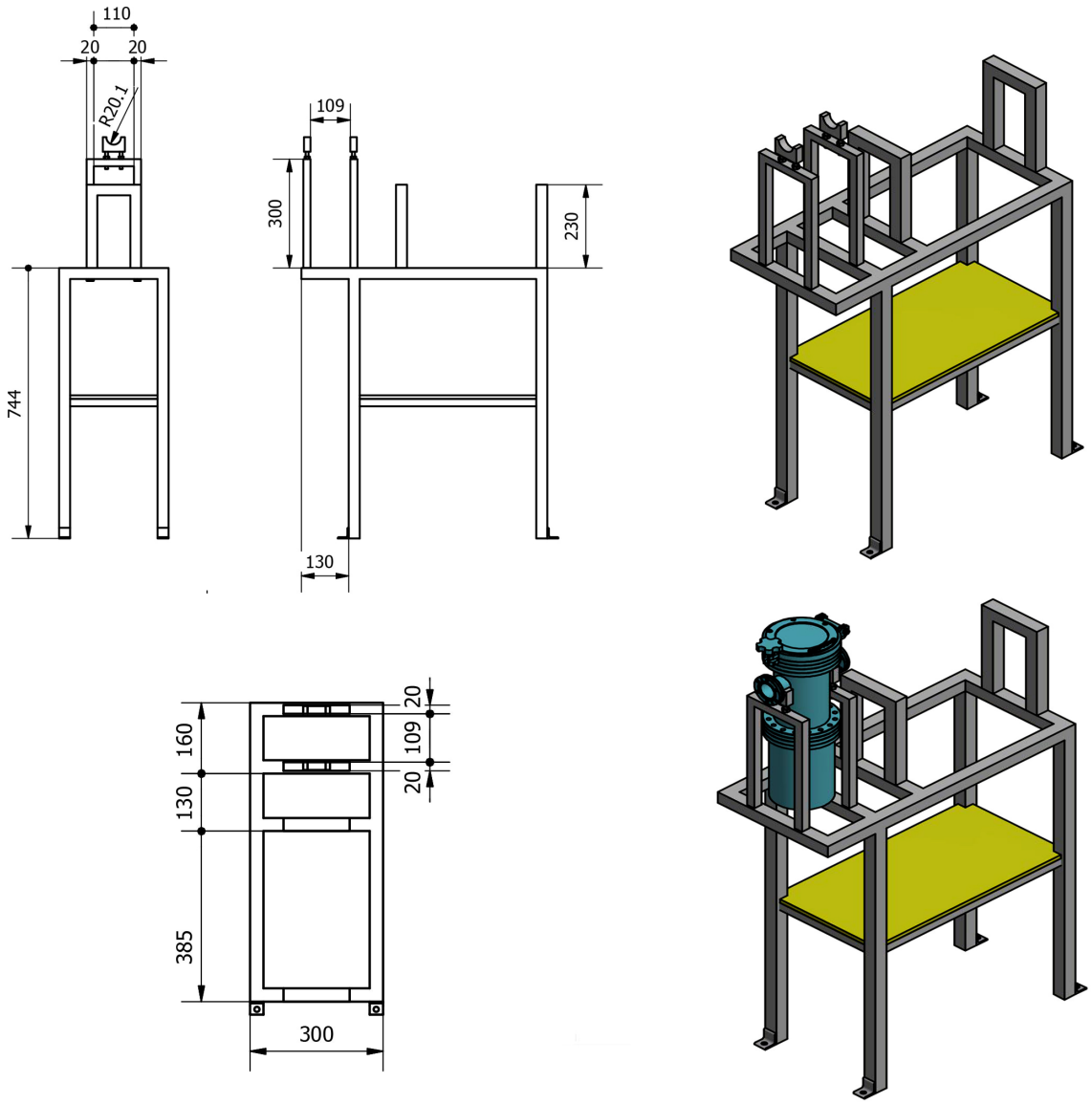

Figure 2.3: Sketches of the introduced load lock chamber with mounting. On the yellow plate underneath the load lock chamber the rotary vane pump is located. On the two mounts behind the LLC a sample transfer system can be placed. The LLC can be adjusted in height to perfectly fit to the flange of the main chamber.

3 Theoretical Background

3.1 Surface Description

To understand the mechanics of helium atom scattering and the surface dynamics of materials a fundamental knowledge of solid state and surface physics is needed. The basic concepts will be explained in the following. More precise explanations can be found in textbooks such as Ch. Kittel's *Introduction to Solid State Physics*[14].
Every crystal is described as a repeating three dimensional arrangement of atoms. To describe the lattice the crystal is divided into unit cells. The unit cell is defined by the three unit cell vectors $(\mathbf{a}_1, \mathbf{a}_2, \mathbf{a}_3)$. To fulfill translational symmetry the positions $\mathbf{r}$ and $\mathbf{r}'$ are indistinguishable if $\mathbf{r}'$ can be described as

$$\mathbf{r}' \;=\; \mathbf{r} \;+\; k \cdot \mathbf{a}_1 \;+\; l \cdot \mathbf{a}_2 \;+\; m \cdot \mathbf{a}_3 \tag{3.1}$$

where (k, l, m) are integers. To get a perfect crystal surface a two-dimensional cut through this ideal bulk crystal has to be performed. Depending on the direction along which the crystal is cut, a specific surface structure is created. In principle a crystal surface must be seen as a three-dimensional object because the top layer atoms are not necessarily arranged within one plane. Nevertheless for the description of the surface lattice two so called *surface unit cell vectors* are sufficient.

$$\mathbf{R}' \;=\; \mathbf{R} \;+\; n \cdot \mathbf{A}_1 \;+\; o \cdot \mathbf{A}_2 \tag{3.2}$$

with (n, o) integers and ($\mathbf{A}_1$,$\mathbf{A}_2$) the *surface unit cell vectors*. In this work surface-specific quantities are depicted using capital letters.

3.2 The Reciprocal Space

When dealing with diffraction experiments the concept of reciprocal space becomes useful. Every unit cell vector can therefore also be defined in reciprocal space using the following equations:

$$\mathbf{A}_1^* \;=\; 2\pi \frac{\mathbf{A}_2 \times \mathbf{n}}{\mathbf{A}_1 \cdot (\mathbf{A}_2 \times \mathbf{n})} \quad , \qquad \mathbf{A}_2^* \;=\; 2\pi \frac{\mathbf{n} \times \mathbf{A}_1}{\mathbf{A}_1 \cdot (\mathbf{A}_2 \times \mathbf{n})} \tag{3.3}$$

where $\mathbf{n}$ is the normalized vector normal to the surface.

This transformation produces a periodic reciprocal lattice. Two reciprocal lattice points $\mathbf{G}$ are connected using the relation

$$\mathbf{G}_{p,q} \;=\; \mathbf{G}_{0,0} \;+\; p \cdot \mathbf{A}_1^* \;+\; q \cdot \mathbf{A}_2^*. \tag{3.4}$$

where p and q are integer numbers called Miller indices. Theses indices are used to define the investigated direction on the surface.

3.2.1 Diffraction from periodic surfaces

From the concept of wave-particle duality every moving particle can be seen as a wave. The momentum of the particle is given by the *de Broglie* wavelength

$$\mathbf{p} \;=\; \hbar \cdot \mathbf{k}, \tag{3.5}$$

When a wave hits a periodic structure diffraction occurs. The wavelength of the wave has to be in the same order of magnitude as the lattice periodicity. The diffraction pattern has various peaks at specific incident angles. These peaks are given by the *Laue-condition*. To fulfill the condition of diffraction the surface-parallel component of incident wave $\mathbf{K}_i$ and the component of the outgoing wave $\mathbf{K}_f$ has to be equal to the reciprocal lattice vector. The total energy during this process is conserved.

$$\Delta\mathbf{K} = \mathbf{K}_f \;-\; \mathbf{K}_i \;=\; \mathbf{G}_{p,q} \tag{3.6}$$

$$E_f \;=\; E_i \tag{3.7}$$

3.3 Helium Atom Scattering

For scattering techniques various particles such as hydrogen, deuterium, electrons, neutrons or helium can be used. However electrons and neutrons penetrate into the bulk and are therefore not strictly surface sensitive. Molecular scattering such as helium scattering only probes the surface of materials. In addition noble gases do not react with the sample and the small particle energy of 10–200 meV leads to a completely non-destructive investigation. Besides measuring the structural properties of the surface of materials the vibronic properties are of great interest. The low mass of the helium atom gives rise to a large cross section for single-phonon interactions. From time-of-flight measurements the phonon energies can be determined. Fig. 3.1 shows several possible processes that can occur when a helium atom hits the surface of a crystalline material.

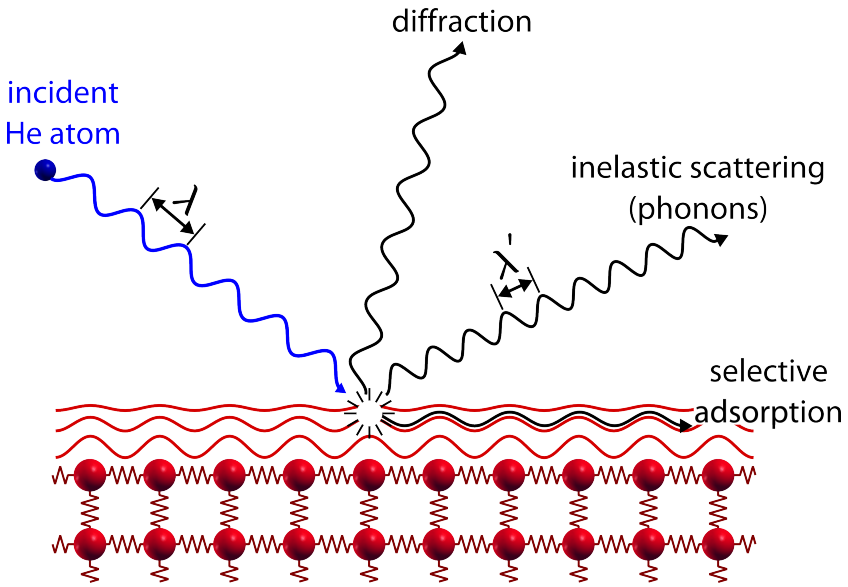

Figure 3.1: Graphical representation of various processes than can occur with He atom scattering. From[2]

3.4 Elastic Helium Atom Scattering

In this work the elastic scattering will only play a minor part. Therefore only a short description is given.
An elastic scattering process happens when the energy of the particle does not change ($E_i = E_f$). The Laue condition 3.7 defines the scattering vector $\Delta\mathbf{K}$ upon diffraction from a periodic surface. The change of momentum during the scattering process has to be equal to a reciprocal lattice vector. Figure 3.2 gives all notations of direction for the scattering process. Apart from the incident vector $\mathbf{k}_i$ the component parallel to the surface is of importance due to the pure surface sensitivity. The angles θ_i, θ_f describe the angle between the incoming/outgoing vector and the z-axis. The sum of these two angles is always constant and given by the source-detector angle θ_{SD}. Simple geometry leads to the parallel components of the wave vector

$$\begin{aligned} |\mathbf{K}_i| &= |\mathbf{k}_i| \cdot \sin(\theta_i) \\ |\mathbf{K}_f| &= |\mathbf{k}_f| \cdot \sin(\theta_f). \end{aligned} \tag{3.8}$$

The azimuth angles ϕ_i, ϕ_i can be changed by rotating the sample along the z-axis. This becomes important for changing the high symmetry orientation.

When combining equations 3.6 and 3.8 the scattering condition is given by

$$\theta_i = \frac{\theta_{SD}}{2} - \arcsin\left[\frac{|\mathbf{G}_{p,q}|}{2|\mathbf{k}_i|\cos(\frac{\theta_{SD}}{2})}\right] \tag{3.9}$$

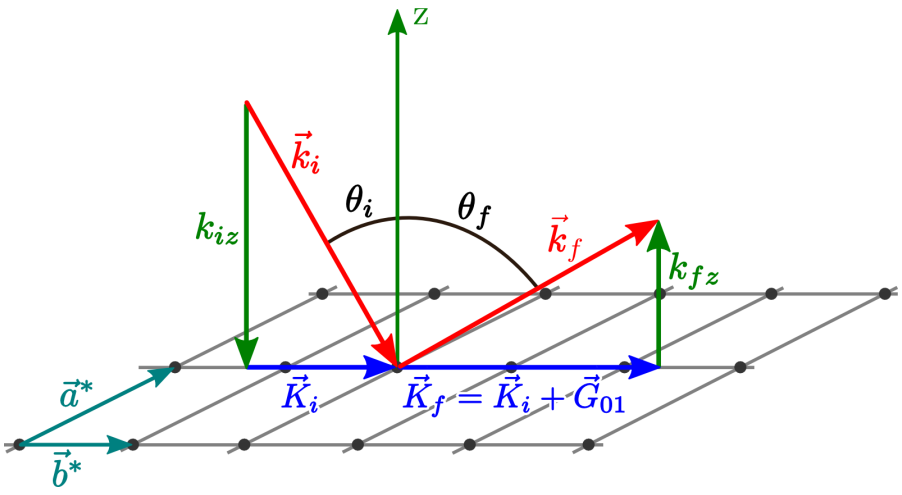

Figure 3.2: Illustration of the scattering geometry of elastic HAS. From[2]

The reciprocal lattice vector can be calculated for a given diffraction angle and wave vector or the reciprocal lattice vector and the respective polar angle can be measured to determine the lattice structure of the sample and therefore get the real space structure.

3.5 Selective Adsorption

Another possible interaction between an incoming helium atom and a surface is the selective adsorption.
Each investigated material has a surface potential, that defines the interaction at the surface. If the incoming helium beam energy is in the same order of magnitude as the potential well depth the attractive well can lead to selective adsorption resonances. This phenomenon has effects on certain disturbances in the intensities of the scattered beam. During this process a helium atom is temporarily trapped in a bound state of the surface potential. After a certain amount of time the helium atom may interact with a **G**-vector of the sample or a phonon and then leaves the bound state of the sample.
This process can be used to determine the atom surface potential of the investigated material.

3.6 Inelastic HAS

As a third process the helium atom can be scattered from the surface inelastically. The main focus of this work will be about the specific surface dynamics, thus the inelastic processes of materials.
Inelastic Scattering occurs when the impinging particle interacts with a quasiparticle

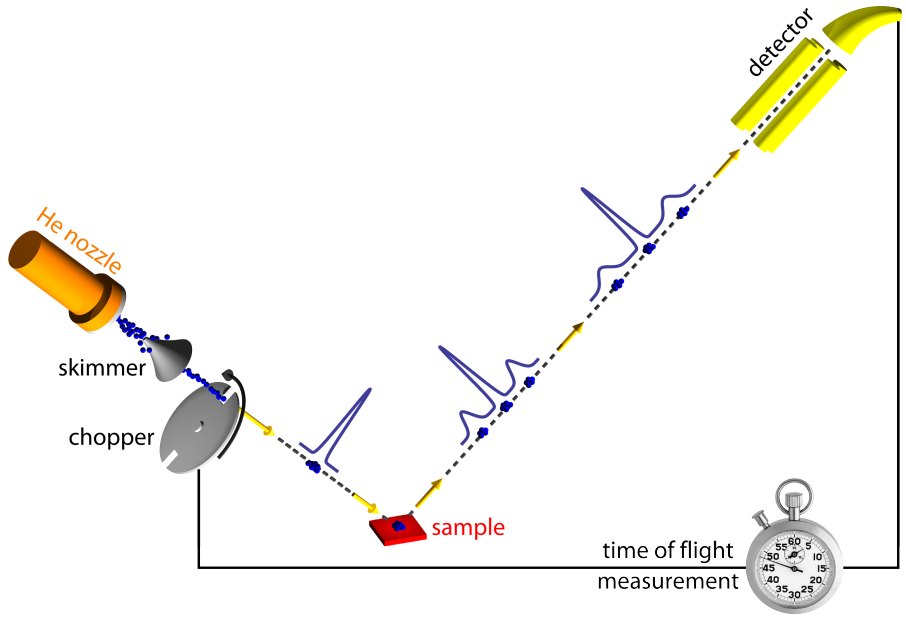

Figure 3.3: Illustration of the basic experimental setup for TOF measurements.[2]

like phonons or plasmons.

3.6.1 Time-of-Flight Measurements

In a time-of-flight (TOF) measurement the time t required for a helium atom to travel a distance L is determined. Knowing these values the speed of the atom can be obtained using:

$$v = \frac{L}{t} \tag{3.10}$$

To get the velocity distribution of a specific beam a so called chopper disk is necessary. This disk chops the helium beam into narrow packets. Bunches with higher velocities are measured earlier at the detector than slower ones. When repeating a lot of measurements a distribution of flight times $g(t)$ is detected. From this result a distribution for velocity $f(v)$ and energy $f(E)$ can be derived[15]. Figure 3.3 shows the basic experimental setup needed to perform TOF measurements. The time it takes for a particle bunch to travel from the chopper disk to the detector has to be measured. To get the velocity given in relation 3.10 the apparatus specific length between chopper and detector has to be exactly known as well.
In a TOF spectrum the width of the peaks defines the resolution. The width depends on the velocity spread of the beam. Another important factor of the resolution is the uncertainty of the flight time which comes into play during the TOF analysis.
One aspect is the finite size of the chopper slits. An ideal transmission function would be a delta function. A better approximation is a trapezoidal function.

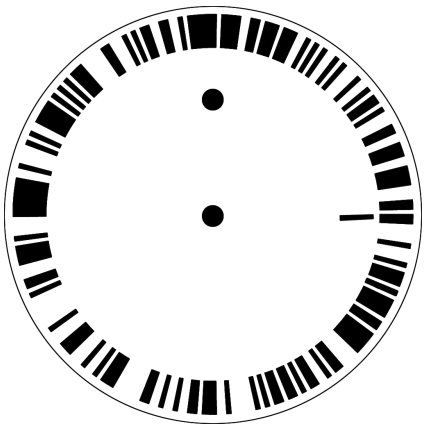

Figure 3.4: Illustration of the pseudorandom chopper disk. The additional slit on the right side is used for synchronisation with the multichannel analyser using a light pulse. The hole in the top has a balancing function.[2]

Another uncertainty is the finite ionization length of the detector. The length between the chopper and the detector can not be exactly defined because the exact point of ionization in the detector is not known precisely. Some helium atoms might be ionized at different points in the detector than others.
Both uncertainties combined give the effective transmission function $T_{eff}(t)$. The measured TOF distribution $G(t)$ includes both uncertainties and is mathematically given by a convolution integral:

$$G(t) \propto \int_{-\infty}^{\infty} T_{eff}(t-\tau)g(\tau)d\tau \tag{3.11}$$

$G(t)$ as well as $T_{eff}(t)$ can be approximated as Gaussian functions which leads to the fact that the deconvoluted TOF distribution $g(t)$ is also of Gaussian form.
To obtain a sufficient signal-to-noise ration the signal of many TOF spectra is integrated over a long time using a multichannel analyser. The chopper disk triggers the start of the multichannel analyser. The corrected time of flight t_f is then given by

$$t_f = t_p - t_c \tag{3.12}$$

with t_p the peak time of the TOF spectra and t_c a correction coming from delayed triggering[15].

Pseudo Random Chopper

To be able to perform TOF measurements the beam has to be cut in smaller packets. This can be done by cutting a slit in a plate and rotating it. However the intensity and therefore the signal to noise ratio would be low. To improve this ratio a pseudo random chopper disk is introduced. For a single slit chopper the intensity of the beam hitting the sample is about 1 %. The pseudo random chopper increases the intensity to

about 50 %. Using such a disk the beam is split into wave packets that are shorter than the spread of the inelastic signal detected. Therefore the TOF spectra from different chopper pulses overlap. Figure 3.5 shows the spreading of the wave packets. Knowing the pulse sequence of the chopper the superposition can be deconvoluted.
The detector has a background $U(t)$. At the detector the distribution $D(t)$ is measured. This signal is a convolution of the desired TOF spectrum $F(t)$ with the so-called shutter function $C(t)$:

$$D(t) = U(t) + (C \odot F)(t) \tag{3.13}$$

with $\odot$ describing the convolution integral:

$$D(t) = U(t) + \int C(t - t'')F(t'')dt'' \tag{3.14}$$

To get the desired distribution $F(t)$ 3.13 is convoluted with the chopper function:

$$F(t) = (C \odot D)(t) - (C \odot U)(t) \tag{3.15}$$

This concept is possible because the cross-correlation function of a random function is a delta function. Therefore the same result is given as if a single slit chopper would have been used. The problem with this approach however is that there is no finite random sequence. To approximate such a sequence a pseudo-random function is introduced. The function is realized with a binary sequence with discrete intervals. The whole length is $N = 2^k - 1$ and the sum of the complete sequence is 1[16]. From this concept the chopper was built as can be seen in figure 3.4.
During an experiment the measured signal $D(t)$ consists of discrete values, that are recorded with a multi channel analyser and deconvoluted. More information about the deconvolution can be found in previous works[3].
This approach to TOF measurements is not suitable for all scenarios. If a TOF spectrum consists of very small peaks combined with very high peaks the statistical noise of the large peaks gets spread over the whole spectrum. After deconvoluting such a signal the tiny peaks are indistinguishable from the background noise. To overcome this error the scattering setup has to be adjusted so that only phonon peaks with similar peak sizes are measured.

Surface Phonons

Phonons are collective quantized excitations in a periodic arrangement of atoms. In quantum mechanics these oscillations are characterized with the Hamiltonian for a harmonic oscillator. The energy for these oscillations with frequency ω is given by:

$$E = \left(l + \frac{1}{2}\right)\hbar\omega \tag{3.16}$$

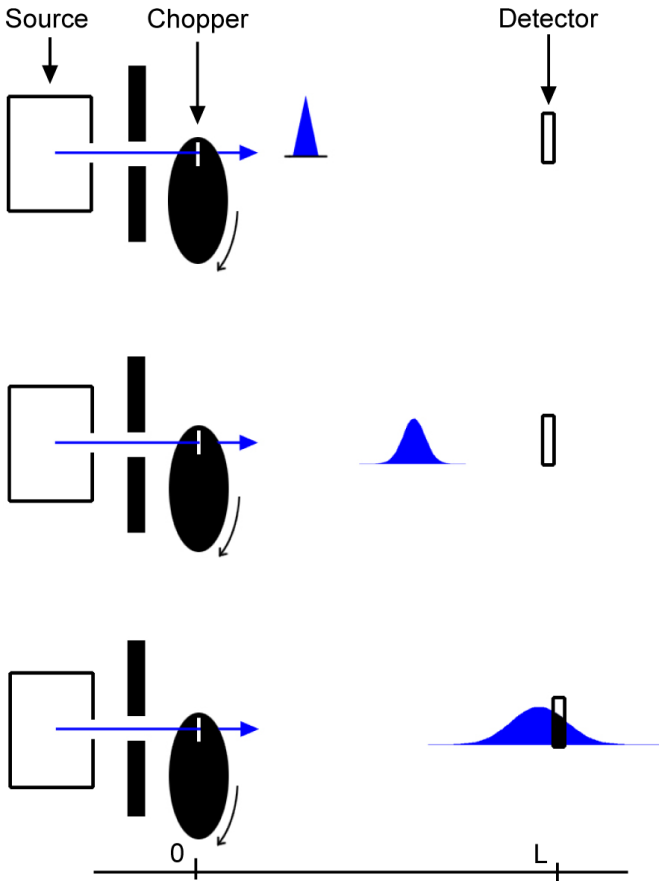

Figure 3.5: Illustration of the dispersion of wave packets. An initial narrow bunch disperses along the way due to the velocity spread of the particles. Therefore various packs overlap at the detector.[3]

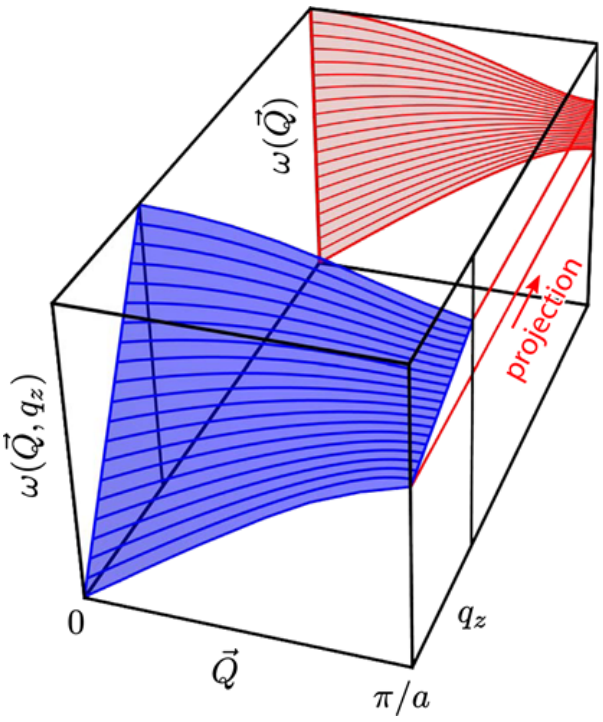

Figure 3.6: Illustration of the projected bulk phonon modes. The 3-dimensional dispersion relation with parallel **Q** are projected onto the surface. The z component is lost and a broad band starts to form from the various bulk modes.[2]

l represents the quantum number and is equal to the number of phonons in that particular state. Physical values such as thermal conductivity or heat capacity strongly depend on these phonon states.
Vibrational modes occurring on surfaces of materials are called surface phonons. Due to breaking the translational symmetry perpendicular to the surface, new eigenstates / solutions of the Schrödinger equation appear.
The surface phonons oscillate like a wave parallel to the surface. This oscillation rapidly decreases into the bulk. Compared to bulk phonons the z-dimension is lost and the states are described with the vector $\mathbf{Q} = (q_x, q_y)$. The z component vanishes when the bulk modes are projected onto the surface. Such a dispersion relation can be seen in figure 3.6.
In general the surface modes are located underneath the bulk modes with respect to frequency. This origins from the number of neighbouring atoms at the surface. The surface atoms experience lower forces due to the missing neighbours along z. The softening of forces affects several uppermost layers. The lowest phonon mode with respect to energy is called Rayleigh mode. It originates from the bulk transverse acoustic band. These oscillations are located in the plane spanned by the surface normal and the propagation direction[17].

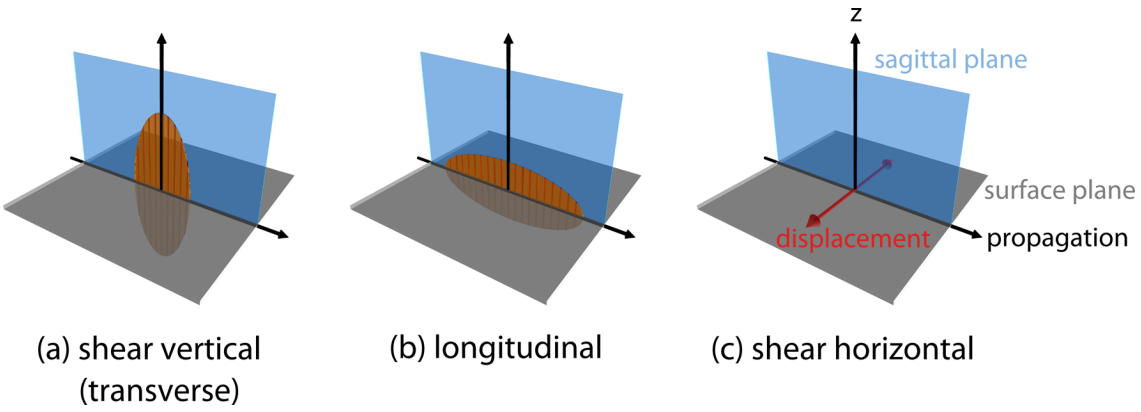

Figure 3.7: Illustration of the three types of surface phonons[19]. (a) shear vertical: The polarization is parallel to the sagittal plane and perpendicular to the propagation direction. (b) longitudinal: The polarization is also parallel to the sagittal plane but in the the propagation direction. (c) shear horizontal: The polarization is in the surface plane, mainly perpendicular to the sagittal plane[2].

Surface phonons are distinguished by their polarization. The plane spanned by the wave vector $\mathbf{k}$ and the surface normal is called sagittal plane (see fig. 3.7).
If a mirror plane of the crystal coincides with the scattering plane only transverse and longitudinal polarized phonons can be measured with HAS. In this work the scattering plane was always along a high-symmetry direction. Therefore the sagittal and scattering plane coincide. In this case shear horizontal modes cannot be excited[18].

3.6.2 From TOF measurements to a surface phonon dispersion

As explained above, TOF measurements are used to determine the change in energy of the scattered helium atoms. From this energy transfer surface phonons can be identified and characterized.
Either the helium atom gains or looses energy during the scattering process. This energy is transferred from or to the surface phonons. In this work only single phonon events are considered. Hence we assume that every inelastic scattering event creates or annihilates one single phonon. Conservation of energy leads to:

$$\begin{aligned} E_f &= E_i + \Delta E = E_i \pm \hbar\omega \\ \frac{\hbar^2}{2m}\mathbf{k}_f^2 &= \frac{\hbar^2}{2m}\mathbf{k}_i^2 \pm \hbar\omega \end{aligned} \tag{3.17}$$

with the subscripts f and i standing for final and initial and $\hbar\omega$ being the energy of the phonon. The plus sign describes an annihilation and the minus sign a creation process. Figure 3.8 illustrates the elastic and inelastic scattering. In addition to conservation of

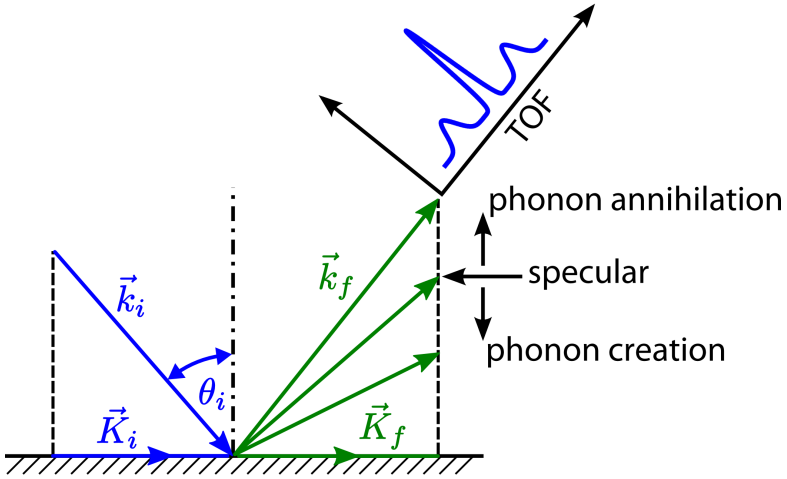

Figure 3.8: Illustration of the elastic (specular) and inelastic scattering process.[2]

energy the parallel momentum has to be constant as well:

$$\mathbf{K}_f = \mathbf{K}_i + \Delta\mathbf{K} \tag{3.18}$$

where $\Delta\mathbf{K}$ denotes the change of momentum of the helium atom during the scattering. In this work we will only consider scattering events in the plane of the surface normal and the incident beam. This assumption leads to

$$k_f \cdot \sin(\theta_f) = k_i \cdot \sin(\theta_i) + \Delta\mathbf{K} \tag{3.19}$$

When combining conservation of energy 3.17 and momentum 3.19 the change in energy ΔE of the phonons can be calculated:

$$\frac{\Delta E}{E_i} + 1 = \frac{\sin(\theta_i)^2}{\sin(\theta_f)^2}\left(1 + \frac{\Delta K}{K_i}\right)^2 \tag{3.20}$$

Equation 3.20 defines the so-called scancurve for the inelastic scattering process. It describes all possible phonon energies ΔE and momenta $\Delta\mathbf{K}$ for a given incident angle θ_i and beam energy E_i. During an experiment θ_i is changed to cover a range of possible ΔK. Continuing this procedure leads to the surface phonon dispersion relation over the whole Brillouin zone. Depending on whether ΔE is positive or negative phonons are created or annihilated at the surface. The change ΔK describes scattering either in the forward or the backward direction.
In the literature phonons are represented with their dispersion curves. These plots show the phonon energy plotted versus the respective phonon wave vector.

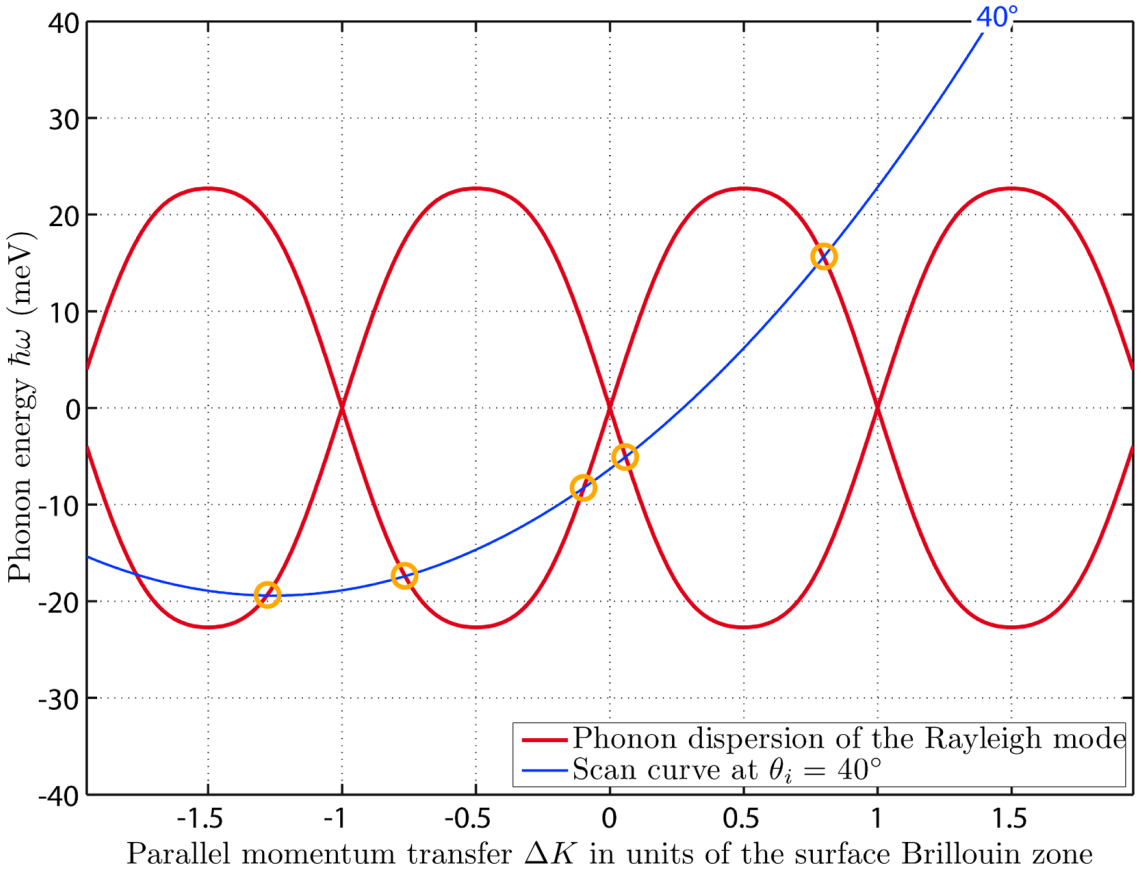

Figure 3.9: Theoretical scan curve for a helium scattering experiment. In blue the specific scan curve for $\theta_i = 40°$ is drawn. The red lines show the phonon dispersion curves. At the intersections of these lines an inelastic peak in the TOF measurement is accessible.[2]

A simplified model in one dimension describes phonons via atoms placed on a linear lattice. Forces between the atoms are represented by elastic springs and the equation of motion can be solved analytically.
In the case of two atoms per unit cell the solution consists of two branches. The energetically lower one is called acoustical and the higher optical branch. This procedure has been treated in greater extend in previous works[20].
For the scan curve the following equation can be arranged:

$$\frac{\Delta K}{K_i} = \sqrt{\frac{\sin^2(\theta_f)}{\sin^2(\theta_i)}\left(\frac{\Delta E}{E_i}+1\right)} - 1 \tag{3.21}$$

The energy of a phonon can be calculated with the simple relation:

$$E = \frac{m}{2}\left(\frac{L_{SD}}{t_{SD}}\right)^2 \tag{3.22}$$

where L_{SD} is the distance between the sample and the detector and t_{SD} the flight time of the inelastically scattered helium atoms from the sample to the detector. This flight time can be expressed via:

$$t_{SD} = t_{CD} - \frac{L_{CS}}{L_{CD}} t_e \tag{3.23}$$

where t_e is the TOF travel time of the elastic atoms between chopper and sample. If the lengths from chopper to detector L_{CD} and from sample to detector L_{SD} are well known the change in energy of the scattered particles can be calculated with:

$$\Delta E = E_i \left[\left(\frac{\frac{L_{SD}}{L_{CD}} t_e}{t_{CD} - \frac{L_{CS}}{L_{CD}} t_e} \right)^2 - 1 \right] \tag{3.24}$$

One can see that the relation between the change in energy ΔE and the TOF t_e is nonlinear[21]. Therefore the heights of the peaks in a TOF spectrum are distorted as can be seen in figure 3.10. To maintain the correct intensity after this variable transformation the signal has to be scaled with the Jacobian determinant:

$$\left| \frac{d\ t_{SD}}{d\ \Delta E} \right| = \frac{t_{SD}^3}{m\ L_{SD}^2} \tag{3.25}$$

This determinant effects the height and the width of the peaks in the energy spectrum. In figure 3.10 one can see that the peaks on the annihilation side become wider and lower. On the creation side the peaks get smaller and higher. On the creation side it is therefore harder to distinguish TOF peaks from background noise.
In addition a change in peak width in the TOF spectrum is caused by two effects. Due to the angular and velocity spread of the helium beam the scan curve has a finite width. Therefore also the TOF spectrum has a finite width. On the other hand the intersection

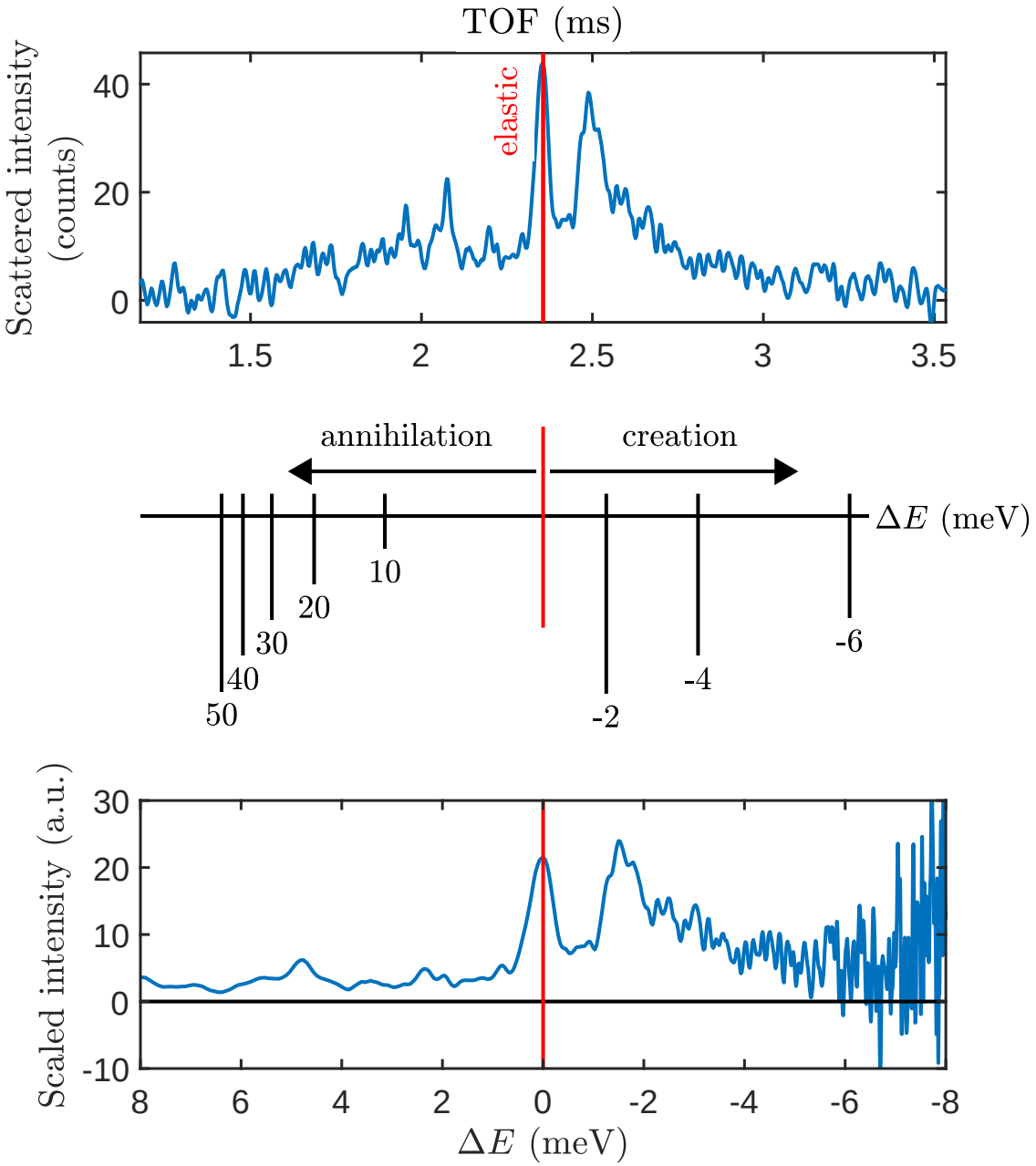

Figure 3.10: Illustration of the conversion of a TOF spectrum (top graph) to energy scale (bottom graph) with equations 3.24 and 3.25. In the middle the non-linearity of this transformation which is later compensated using the Jacobian is shown. However this Jacobian also changes the height of the peaks and therefore the experimental noise is increased. The spectrum is depicted from a measurement of Bi_2Se_3 in the $\overline{\Gamma M}$ direction with an incident angle of $\theta_i = 41.75°$ an incident energy of $E_i = 10.16\,\text{meV}$ and a sample temperature of 295 K.

angle between the scan curve and the dispersion plays an important role as well. The phonon peak has the smallest width if the scancurve crosses the dispersion curve at an angle close to 90°. The resolution is worst when the scan curve is tangent to the dispersion curve. This leads to an effect called kinematical focusing which shows also up in the elastic spectrum[22].

3.7 Debye-Waller Factor

All theoretical treatments of the scattering processes described so far assume that the atoms of the sample are at complete rest and therefore a perfect periodic crystal structure is formed. However at finite surface temperature in addition to zero-point motion thermal vibrations appear. These vibrations lead to additional inelastic scattering during a scattering event.
The effect can be seen in the thermal attenuation of the elastic diffraction intensities. The peak shapes stay the same however. The attenuation is described by

$$I(T_S) \;=\; I_0 \cdot \mathrm{e}^{-2W(T_S)} \tag{3.26}$$

with $I(T_S)$ being the diffraction intensity at the sample temperature T_S and I_0 the intensity at rest. In the exponent $W(T_S)$ is the so-called *Debye-Waller factor* and defined as

$$2W(T_S) \;=\; \left\langle (\mathbf{u}\cdot\Delta\mathbf{k})^2 \right\rangle_{T_S}, \tag{3.27}$$

with $\mathbf{u}$ being the displacement vector of a lattice atom out of its thermal equilibrium position and $\Delta\mathbf{k}$ the total change in momentum of a scattered particle during a scattering event. The angle brackets indicate that the thermal average is taken[15]. For the specular contribution, the momentum transfer parallel to the surface equals zero. This approximation reduces 3.27 to:

$$2W(T_S) \;=\; \left\langle u_z^2 \right\rangle \cdot (\Delta k_z)^2, \tag{3.28}$$

with $\langle u_z^2 \rangle$ describing the average squared atomic displacement perpendicular to the surface. In a first approximation the vibrations can be treated like a harmonic oscillator. $\langle u_z^2 \rangle$ can then be described by

$$\left\langle u_z^2 \right\rangle \;=\; \frac{3k_\mathrm{B}T}{M\omega^2} \tag{3.29}$$

with M the effective mass of the surface atoms. Using the Debye model, the vibrational frequency ω is described by the Debye frequency

$$\omega_D \;=\; \frac{k_\mathrm{B}\theta_D}{\hbar} \tag{3.30}$$

with θ_D the *Debye temperature*. Combining all equations the Debye-Waller (DW) factor becomes

$$W(T_S) = \frac{3\hbar^2 T_S}{2M k_B \theta_D^2} \Delta k_z^2. \tag{3.31}$$

In a more realistic model the attractive part of the atom-surface potential has to be considered. The attractive part of the potential leads to an acceleration of the incoming helium atom and a deceleration of the scattered atoms when they leave the surface potential.
This effect is taken into account in the Beeby-correction. To describe this attraction the energy of the well depth D is added to the incident beam energy. The new perpendicular momentum transfer is given by:

$$\Delta k_z = k_i \left[\sqrt{\cos^2(\theta_f) + \frac{D}{E_i}} + \sqrt{\cos^2(\theta_i) + \frac{D}{E_i}} \right] \tag{3.32}$$

The well depth is usually assumed to be between 4–10 meV for helium atom scattering. The Beeby-correction is now applied to 3.31 by replacing Δk_z with equation 3.32. For the specular beam $\theta_i = \theta_f$ holds which leads to the expression:

$$W(T_S) = \frac{12m \left[E_i \cos^2(\theta_i) + D\right]}{2M k_B \theta_D^2} T_S \tag{3.33}$$

where m is the mass of the impinging particle.
For a more accurate description of the thermal attenuation multi-phonon precesses have to be taken in consideration which will not be treated in this work[23].

4 Topological Insulators & sample preparation

The field of topological insulators (TIs) brought a whole new classification paradigm to the field of condensed matter and electronic materials. Three-dimensional topological insulators are a new state of quantum matter with a bulk gap and an odd number of relativistic Dirac fermions on the surface[24,25]. Therefore they are insulating in the bulk but conducting at their boundaries. These boundary states are protected by time-reversal symmetry and the carriers order themselves in a way that there is spin-momentum locking. The direction in which the carriers are travelling defines the orientation of the spin. This phenomenon is an analogy to the Quantum Hall effect: The description of using topological invariants showed that the Quantum Hall conductance can only take certain values that are integers of e^2/h. This introduces a severe constraint on the motion of the charge carriers. A similar conductance quantization was predicted for the spin degree of freedom in 2 dimensional topological insulators. These materials can be viewed as two superimposed Quantum Hall phases in which the spin-orbit interaction functions as an effective magnetic field that acts in opposite directions for opposite spins. Therefore charge carries on the surface with spin up move in the opposite direction of carriers with spin down. Because of this behaviour 2D topological insulators are described as Quantum Spin Hall phases. The first materials to show this Quantum Spin Hall phase were graphene as well as cadmium telluride/mercury telluride/cadmium telluride (CdTe/HgTe/CdTe) quantum wells. In this device a 7 nm thin sheet of HgTe is put between two CdTe sheets.

The next materials to follow were 3D bulk solids of binary compounds involving bismuth[26]. The energy dispersion of these materials exhibits a Dirac cone at the Γ-Point. In three-dimensional TIs the low-energy electronic properties are dominated by massless Dirac Fermion excitations, where the energy dispersion relation is described by a Dirac cone. In figure 4.3 such a Dirac cone is shown in the case of Bi_2Se_3. The Fermi level lies in the small bandgap. In-between the bulk conduction band and the bulk valence band surface states appear that fall within the bulk energy gap. The interrupted symmetry at the surface produces these surface specific bands which cross the Fermi energy[27] (see figure 4.1).

This new class of materials opens new horizons for using the spin degree of freedom in future information precessing technologies which are called spintronics. These spintronic

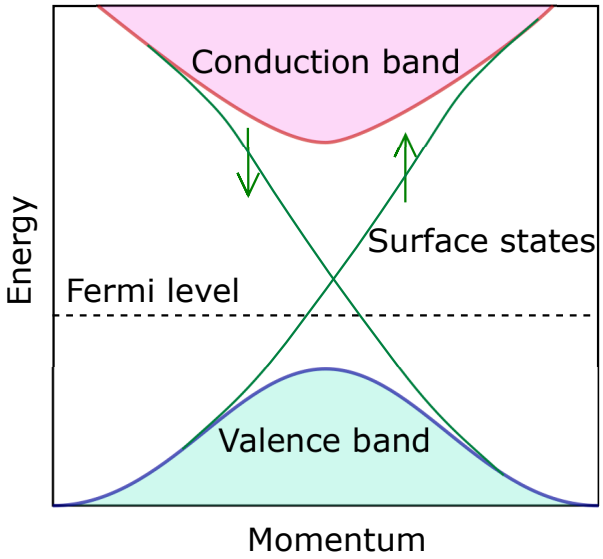

Figure 4.1: Bandstructure of Topological Insulators. The Fermi level lies in-between the conduction and the valence band. The interrupted symmetry at the surface of topological insulators produces surface specific bands which cross the Fermi energy.

devices include spin filtering, spin control and magnetic recording technologies. Large spin torques can be used for memory devices, which leads to lower power consumption and capabilities of replacing conventional electronics to quantum computing. TIs could be further used for flexible electronics[28], nonlinear optics or as efficient thermoelectric materials. Bi_2Se_3 and Bi_2Te_3 are some of the best preforming thermoelectric materials[29].

4.1 Properties of Bi_2Se_3

Bi_2Se_3 is one of the most prominent materials from the class of 3D topological insulators. The interaction of surface phonons with electrons on Bi_2Se_3 has been studied intensively with relation to the electron-phonon (e-ph) coupling constant λ[30–35]. Since scattering channels for the surface state electrons may impose constraints for potential applications such as surface-dominated transport, a major objective on the way to technical applications[36], λ is a convenient parameter to characterize e-ph interaction strength.
However, very little experimental data exists for the surface phonon dispersion of $Bi_2Se_3(111)$. In general the region of acoustic phonon modes on topological insulator surfaces has not been investigated intensively. Bismuth selenide is also a classic thermoelectric material with a large Seebeck coefficient[37,38].
To fully understand the thermoelectric properties of Bi_2Se_3 films and the low lattice ther-

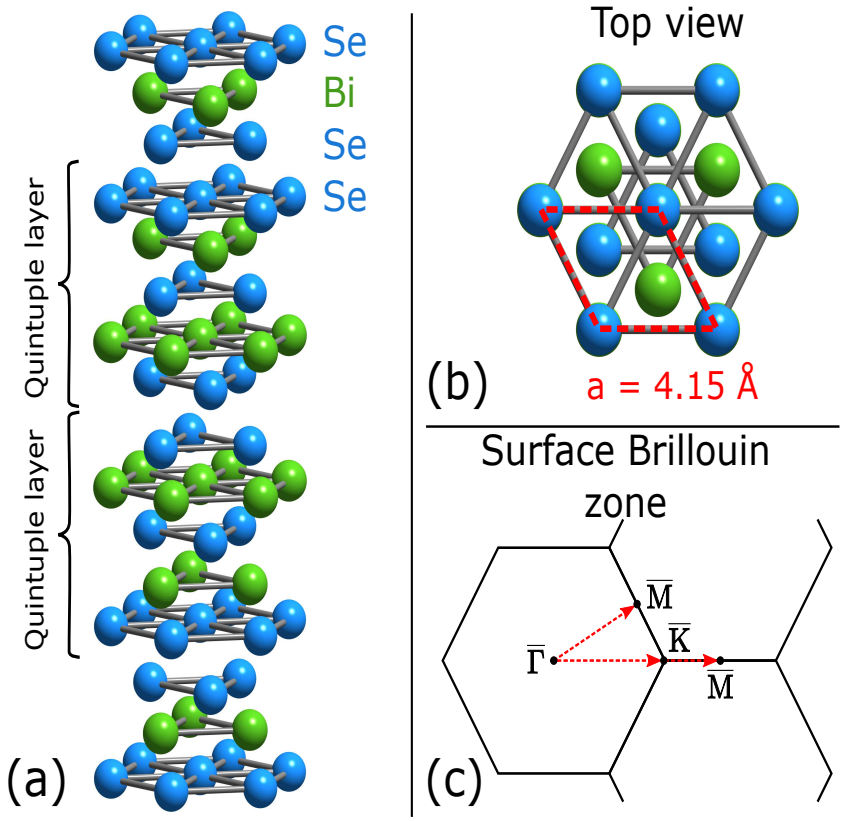

Figure 4.2: (a) Graphical impression of the hexagonal unit cell of the Bi_2Se_3 crystal. The unit cell consists of three quintuple layers of which each one is terminated by a Se layer. (b) Top view of the (111) surface of Bi_2Se_3 where the red rhombus highlights the hexagonal surface unit cell with the lattice constant a. (c) Surface Brillouin zone with the two high symmetry scanning directions.

mal conductivity of Bi_2Se_3 the information on the surface phonon dispersion is crucial. Because of their large Seebeck coefficient Bi_2Se_3 has been used in thermoelectric refrigeration for a long time[39]. The excellent thermoelectric performance of Bi_2Se_3 has been attributed to the details of the electronic structure and a low thermal conductivity[37]. Previous to this work the acoustic phonons of this material have only been investigated by one group[40], which could not resolve the phonon dispersion over the entire Brillouin zone.

In figure 4.2 the hexagonal unit cell of Bi_2Se_3 is shown. The hexagonal lattice has a lattice constant of $a = 4.15\,\text{Å}$. The crystal consists of a layered material which is ordered in quintuple layers consisting of Bi and Se. Theses layers are weakly bonded by van der Waals forces. Therefore the whole material is easy to cleave.

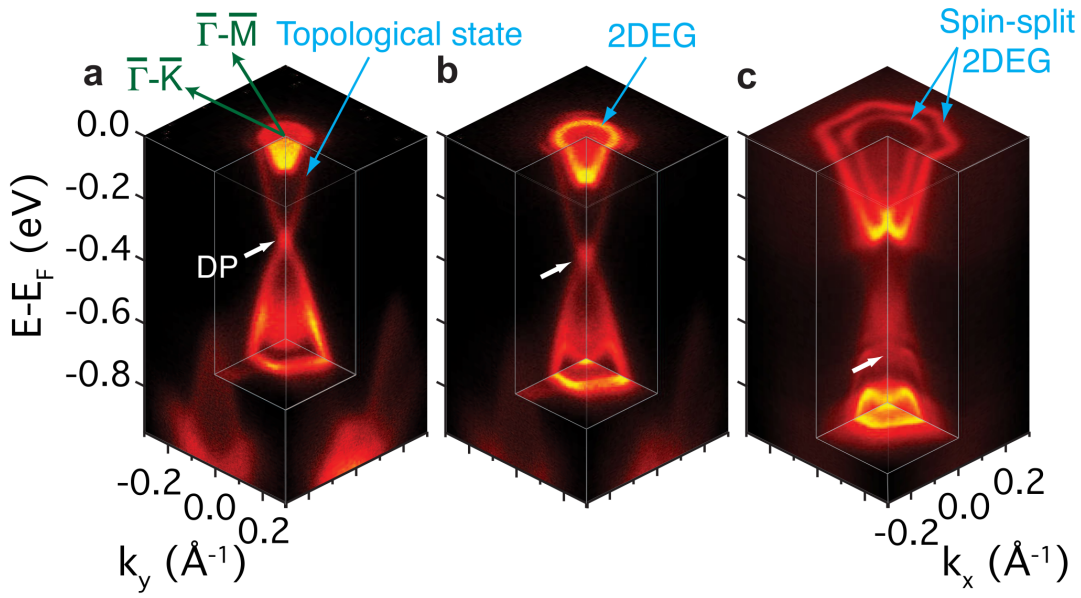

Figure 4.3: Electronic structure of Bi_2Se_3 measured using time-of-flight ARPES at increasing times after cleaving the sample.[41]

The electronic structure of Bi_2Se_3 is shown in figure 4.3. In 4.3a the freshly-cleaved sample shows the linearly-dispersing topological surface state with its Dirac point. Near the Fermi level, occupied bulk conduction band states are visible. After some time, the Dirac point shifts to higher binding energies, resulting in a quantum well that causes a 2D electron gas (2DEG) to form at the surface. With further surface doping a well-defined spin splitting of the states is established[41].

4.2 Sample Preparation

The Bi_2Se_3 crystal was grown at the Center for Materials Crystallography (Department of Chemistry and iNANO) at Aarhus University in Denmark in a two-step process. First, stoichiometric mixtures of 5N purity elemental Bi and Se were melted in an evacuated ampoule at 860 °C for 24 h. The obtained products were then checked by X-ray diffraction and the synthesis of the compound was confirmed. In a second step, the single crystal was grown by slowly heating the obtained compound inside an evacuated and sealed quartz ampoule followed by annealing at 650 °C for 10 days.

Fig. 4.4 shows the sample before the sample preparation. To be able to put the sample into the manipulator the sample had to be fixed onto a sample holder. The sample was attached to the sample holder using thermally and electrically conducting Epoxy EPO-TEK H21D. The two Epoxy components were mixed in the ratio 10:1 by weight. A small amount was placed on the sample holder and the sample was carefully pressed

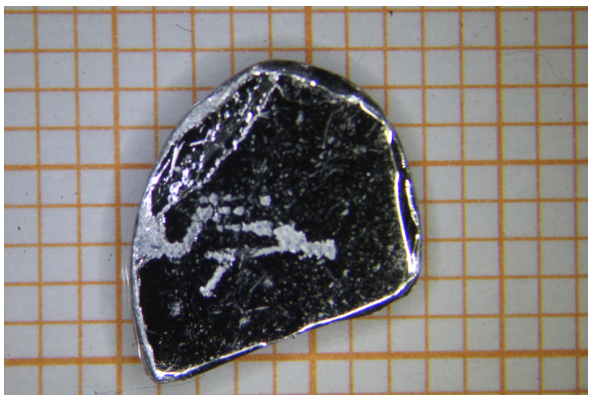

Figure 4.4: Bi_2Se_3 Sample in its early condition before the sample preparation. One square of the background represents 1 mm^2.

onto it. To cure the epoxy the sample was baked in an oven for 15 minutes at 130 °C. For helium atom scattering a flat sample is needed. Therefore the rough surface had to be flattened. This was realized by using the scotch tape method. By applying a scotch tape evenly on the surface and pulling it off into one direction a smooth surface can be achieved.
The sample holder was then put into the gripper of the load lock chamber. (see chap. 2) Once again a scotch tape was applied on the surface and on the transfer chamber wall. Under evacuated conditions the surface was peeled off *in-situ* by moving the gripper away from the chamber wall. Using this method surface contamination can be held at a minimum.

5 Elastic Scattering - Results and analysis

This chapter treats the elastic measurements preformed for the initial characterization of the material. The results are important for further inelastic investigations.

5.1 LEED

To get a first impression of the orientation and cleanness of the sample a LEED experiment was performed. For this analysis the sample was moved to the top of the main chamber where the LEED is located and the LEED control unit was switched on. After adjusting the beam energy of the LEED to $\sim$29 eV diffraction spots became visible on the screen. For the following scattering experiments it is crucial to have the sample perfectly oriented into the high symmetry directions. To get the ideal orientation of the sample the azimuthal angle was adjusted while looking at the LEED picture. The LEED picture of the Bi_2Se_3 crystal aligned along the high symmetry orientations can be seen in fig. 5.1.

5.2 θ-scans

After the first characterization of the sample using LEED, elastic scattering measurements were performed. In an elastic measurement the incident energy E_i and sample temperature T_S are held constant while the incident angle θ_i is changed. By changing the incident energy E_i the diffraction peaks change the position relative to the specular peak. This change in position can be seen in figure 5.2. For lower beam energies the first order diffraction peaks are further away from the zero order peak.
The top plot in figure 5.2 shows a scan in the high symmetry direction $\overline{\Gamma\mathrm{M}}$. In this direction better counting rates have been achieved compared to the $\overline{\Gamma\mathrm{K}}$ azimuth. The very sharp peaks are an indication of the good quality and flatness of the crystal.
In the bottom plot of figure 5.2 an elastic scan in $\overline{\Gamma\mathrm{K}}$ direction is depicted. The left first order diffraction peak appears rather low. This may come from a misalignment in the tilt of the sample. For these θ-scans the tilt of the sample plays an important role since the sample itself is rotated during a measurement (see apparatus setup in 2.1).

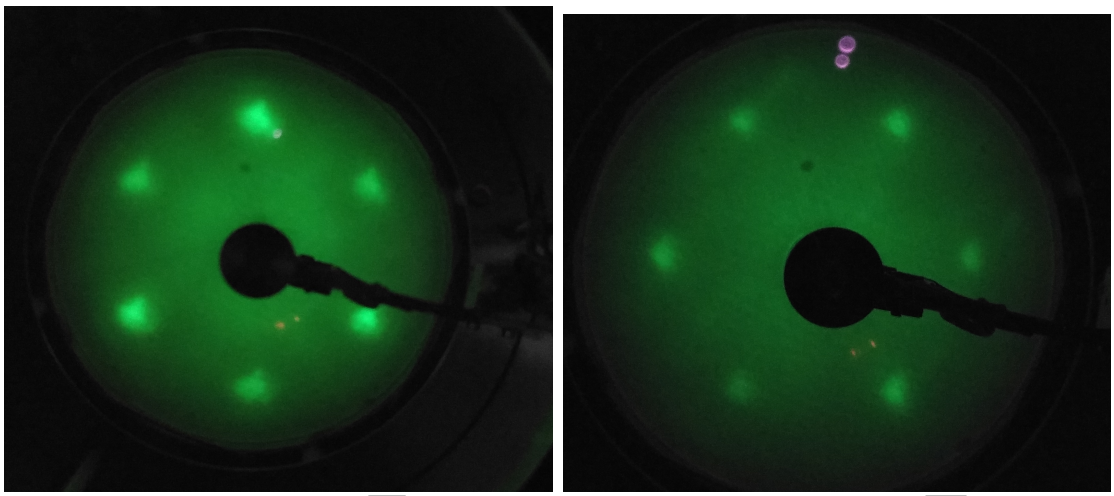

(a) LEED picture $\overline{\Gamma K}$ (b) LEED picture $\overline{\Gamma M}$

Figure 5.1: LEED picture of the investigated hexagonal crystal Bi_2Se_3. (a) shows the orientation in the high symmetry direction $\overline{\Gamma K}$. Note that the first Brillouin zone is rotated again by 30° compared to this pattern. (b) shows the crystal in the symmetry orientation $\overline{\Gamma M}$

From the distance between the elastic scattering peaks the lattice constant can be calculated. If the difference between the incoming parallel momentum $\mathbf{K}_i$ and the outgoing parallel momentum $\mathbf{K}_f$ is exactly the lattice constant (see equation 3.7) a diffraction peak appears at this specific incident angle θ_i. In figure 3.2 the scattering geometry is illustrated. If the incident angles at which a diffraction peak arises are defined from the experiment and the beam energy is know the lattice constant can be calculated.
Different elastic spectra with various beam energies in both high symmetry directions and the sample cooled to 115 K were compared. Taking the average value the lattice constant was determined to be:

$$a = (4.14 \pm 0.01)\,\text{Å}$$

In the literature the bulk lattice constant for a sample temperature of 115 K is given as $a = 4.129\,\text{Å}$ [42].
During the analysis of various elastic spectra the lattice constant varied from 4.11 to 4.17 Å depending on the sample temperature. Due to the thermal expansion of the crystal, measurements with the sample cooled down to 123 K tended to have lower lattice constants compared to elastic scans with the sample held at room temperature.

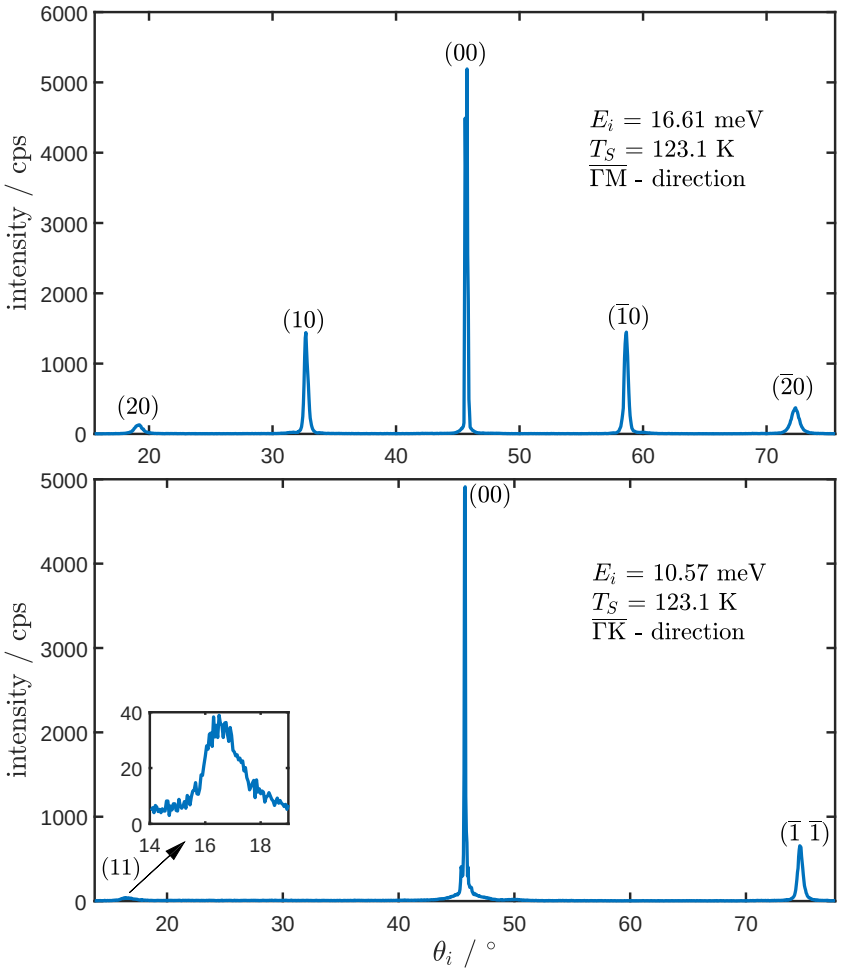

Figure 5.2: Plot of the elastic spectrum in $\overline{\Gamma M}$ and $\overline{\Gamma K}$ direction. In the top plot diffraction peaks up to the second order can be seen. In the bottom plot the incident energy E_i is lower and therefore the first order diffraction peaks are further away from the specular peak. In addition the lattice vector G_{11} is bigger than G_{10}.

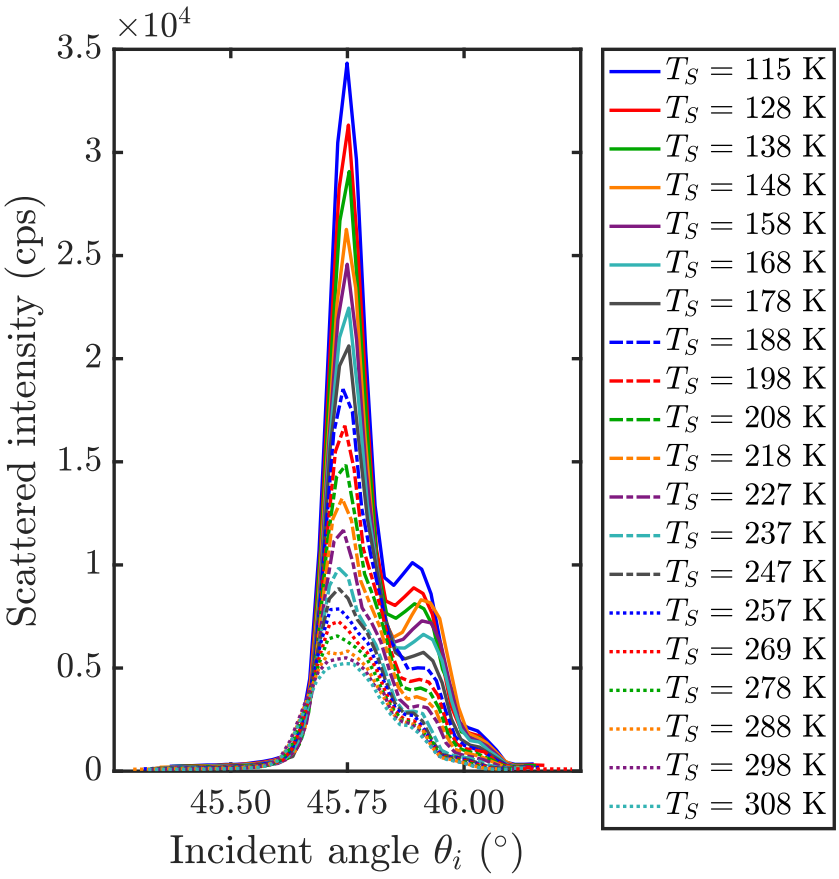

Figure 5.3: Plot of thermal attenuation of the specular peak with changing surface temperature of Bi_2Se_3. The measurements were taken with a beam energy of 9.98 meV.

5.3 Surface Debye Temperature / Debye-Waller Factor

To get a first insight into the surface vibrational dynamics the thermal attenuation of the diffraction peaks was measured.
In figure 5.3 the change of the specular peak intensity due to the increasing surface temperature can be seen. To get this picture several elastic scans around the zero order diffraction peak with a helium beam energy of $E_i = 9.98$ meV were taken. For the different measurements the sample temperature was changed between 115 K and 308 K.
Due to the increase in surface temperature, inelastic scattering of the incoming helium atoms becomes more likely. The vibrational modes of the surface atoms lead to this attenuation which is described by the Debye-Waller factor (see chapter 3.7).

In figure 5.3 in addition to the specular peak a shoulder can be seen. This side-peak may be a sign of a selective adsorption effect (chapter 3.5). The attractive potential well can lead to selective adsorption resonances which causes certain disturbances in the

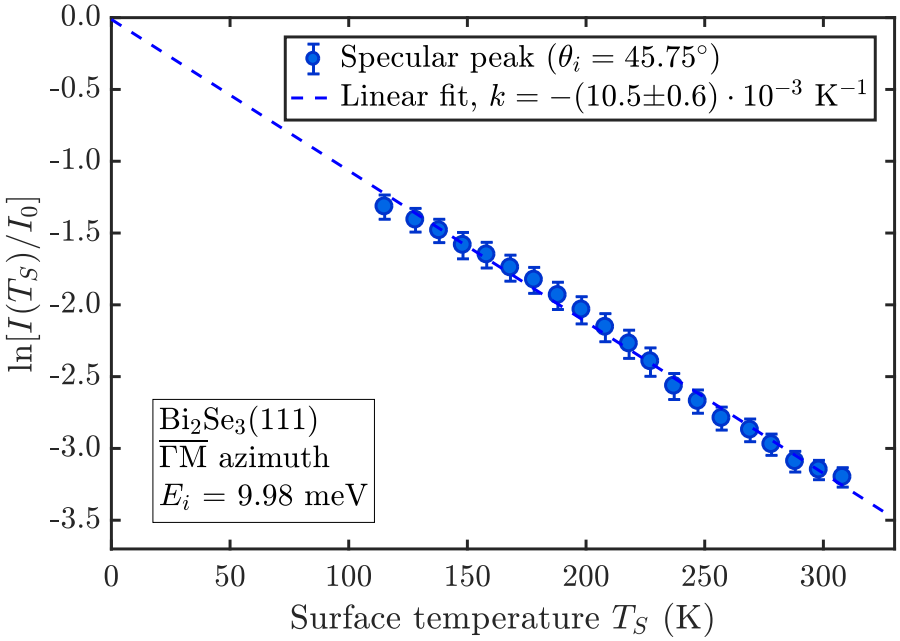

Figure 5.4: Plot of the decay of the specular peak intensity versus the sample surface temperature due to thermal attenuation. To get this linear slope the logarithm of the intensity ratio $I(T_S)/I_0$ was taken. The incident beam energy was held at 9.98 meV.

intensities of the scattered beam. These resonance effects also decrease with increasing sample temperature because the inelastic effects start to overcome the elastic ones.
The logarithm of the intensity ratio $\ln(I(T_S)/I_0)$ plotted versus the surface temperature T_S follows a linear decay. In the Debye model the surface Debye temperature can be extracted from the slope of this plot. In figure 5.4 the decay of the intensity of the specular peak is plotted. All measurements have been taken with the sample oriented in the high symmetry direction $\overline{\Gamma M}$.

The experimental data are in good agreement with the linear decay within its uncertainties. The small deviations might be caused by a deviation from the Debye model (onset of optical modes) as well as small misalignments of the sample. The sample position changes due to elongation of the liquid nitrogen cooled parts of the manipulator and mist therefore be realigned.
The linear fit in figure 5.4 has a slope of $(-10.5 \pm 0.6) \times 10^{-3}\,\mathrm{K}^{-1}$. Knowing the slope (Debye-Waller factor) $W(T_S)$, the incident energy E_i and the incident angle θ_i equation 3.33 gives the Debye temperature θ_D. However, the mass of the surface atom scatterer M and the potential well depth D have to be known as well. Since the uppermost layer of the sample consists of a layer of selenium atoms (see figure 4.2) in first approximation the atomic mass of selenium was taken for M. From previous elastic scattering measurement and the analysis of the selective adsorption events the potential well was

determined to be $D = 4.8\,\mathrm{meV}$.
Using these values the surface Debye temperature was determined to be

$$\theta_D = (114 \pm 6)\,\mathrm{K}$$

. When compared with the bulk value of $(182 \pm 3)\,\mathrm{K}$[43] the surface Debye temperature is reduced significantly. This is in good agreement with the assumption of van Delft that the surface Debye temperature is smaller compared to the bulk value by a factor of $1/\sqrt{2}$[44].
However the scatter mass M is not necessarily the exact mass of a single Se atom. Considering that the impinging helium atoms not only interact with the uppermost layer of selenium the second layer of bismuth has to be taken into account as well. This would lead to an *effective* scatter mass M^*. The atomic mass of Bi (208.9 u) is much higher than the one for Se ((78.9 u)). Taking into account that the lighter Se atoms are more likely to oscillate an effective scatter mass M^* of 120 u can be defined. This value would lead to a surface Debye temperature of $(92 \pm 5)\,\mathrm{K}$.
Since the effective mass can not be defined exactly it is much more practical to define the value $\alpha = \theta_D^2 \cdot M$ which is the product of the surface Debye temperature squared and the scatter mass. Using equation 3.33, α is given by

$$\alpha = \frac{12m\,[E_i \cos^2(\theta_i) + D]}{2k_\mathrm{B}k} \tag{5.1}$$

with k being the slope of the logarithmic plot as seen in 5.4.
For Bi_2Se_3 the value is $\alpha = (1.69 \pm 0.09) \times 10^{-21}\,\mathrm{K^2\,kg}$.
Up to this date no other literature values for the surface Debye temperature of Bi_2Se_3 were listed.
Previous works on graphene monolayers and metal substrates in terms of the Debye temperature corresponding to the surface normal vibration have shown similar difficulties defining the correct surface effective mass[45].

6 Inelastic Scattering - Results and analysis

In this part all performed TOF measurements on the material Bi_2Se_3 are shown and discussed. The procedure of obtaining the surface phonon energies is described below.

6.1 Time of Flight Measurements

After each TOF measurement the signal from the multichannel analyser is deconvoluted and converted into an energy scale as described in section 3.6.2. In a first example a converted TOF spectrum is shown in figure 6.1(a).
In addition to the transformation to energy scale another mathematical step has been taken to further improve the appearance of the TOF spectrum. In figure 6.1(a) a black and a grey line are plotted. The grey line represents signal versus energy which becomes very noisy at the creation side with increasing energy. Due to the non-linear transformation to energy, the data points are no longer equally spaced and the distance between two data points decreases with decreasing ΔE. Therefore experimental noise will increase on the creation side making it difficult to distinguish peaks from noise.
To overcome these strong oscillations a binning was performed. Hence averages were taken over small energy intervals with increasing sample width on the creation side to smooth the line. The black line shows that signal after the binning was performed.
The measurement was taken in the high symmetry direction $\overline{\Gamma\mathrm{M}}$ with an incident angle of $\theta_i = 41.75°$ and a sample temperature of 295 K. The nozzle temperature was held at 50 K which (with equ. 2.3) leads to an incident energy of $E_i = 10.16\,\mathrm{meV}$. The TOF spectrum consists of various peaks which are located on the creation (negative x-axis) as well as the annihilation (positive axis) region. In between at zero energy transfer the intensity of the elastically scattered helium atoms can be seen.
To get an idea which phonons with specific energies were created/annihilated one has to identify peaks in the TOF spectrum. It is important to compare various spectra in order to decide whether a certain peak is significant or not. It is always important to keep in mind that the scaling of the peaks changes during the energy transformation (as described above in fig. 3.10). Therefore the lower peaks on the positive side are still as significant as the higher ones on the left side.

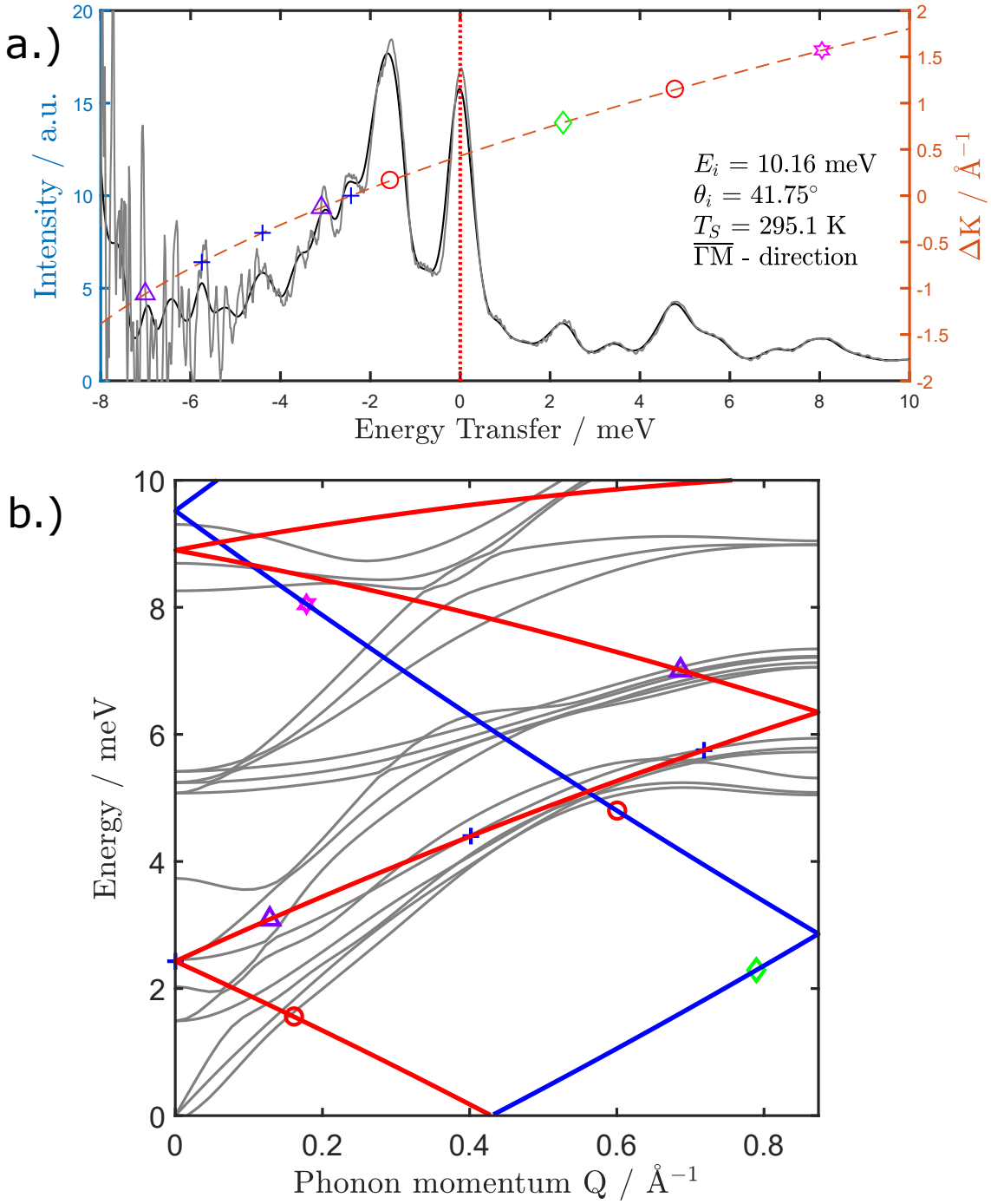

Figure 6.1: Plot of the performed TOF measurements. In (a) the TOF spectrum with the x-axis converted to energy is shown. The vertical red line symbolizes the elastically scattered atoms. In (b) the corresponding scan curve folded back into the first Brillouin Zone is plotted. In the background the theoretical calculations done with DFPT are drawn.

The right y-axis in figure 6.1(a) associates each phonon with a specific momentum transfer ΔK (equ. 3.22). The incoming helium atom looses or gains momentum during the scattering process which is transferred to a phonon. However a reciprocal lattice vector G_{hk} can be added or subtracted.

$$\Delta \mathrm{K} = \mathrm{Q} \pm G_{hk} \tag{6.1}$$

where Q is the phonon momentum. This relation is only valid for the assumption of only single phonon events.
Once the energy transfer values for each peak are defined, one has to look at the scan curve for this specific incident angle θ_i and energy E_i. In figure 6.1 (b) the scan curve is plotted as energy versus the phonon momentum Q. Compared to the plot in the theoretical introduction 3.9 the scan curve is now folded back into the irreducible Brillouin zone. This compensates the addition of a lattice vector G_{hk} from equation 6.1. The scancurve has also been folded from negative up to positive energies. This is possible since the phonon dispersion is defined in the irreducible part of the Brillouin zone and all phonon events can be projected back into the irreducible Brillouin zone. In the figure the scan curve consists of a red branch representing the annihilation of a phonon and a blue branch for the creation of a phonon.
In figure 6.1 (a) we see a strong peak at about $-1.8\,\mathrm{meV}$ in the creation part. Therefore one has to look at the red line in the scan curve and go to the same value on the y-axis. In figure 6.1 (b) we see the scan curve as well as the theoretical calculation of the phonon dispersion curves using DFPT (Density Functional Perturbation Theory). Here a peak at $\Delta E = 1.8\,\mathrm{meV}$ would correspond to a momentum transfer $\mathrm{Q} = 0.15\,\mathrm{\AA}^{-1}$ according to equation 3.21. Now we see that the red line is crossing several branches of the theoretical calculation at a y-value of around 1.8 meV.
Since the red line crosses the lowest dispersion branch, these phonons are part of the Rayleigh mode (see chapter 3.6.1).

6.2 Elastic Effects in Inelastic Measurements - Deceptons

It may happen that a strongly defined peak arises in the TOF spectrum even though the scan curve is not crossing any lines of the calculated phonon dispersion. These anticipated phonons however originate from elastic effects during the inelastic measurement. Such events are called deceptons or spurions due to their misleading nature[46].
The incident helium beam coming from the nozzle of the source arm has a certain velocity distribution. The wings of this distribution with a velocity v^* have significantly different elastic diffraction properties. Compared to the average velocity v_0 the time of

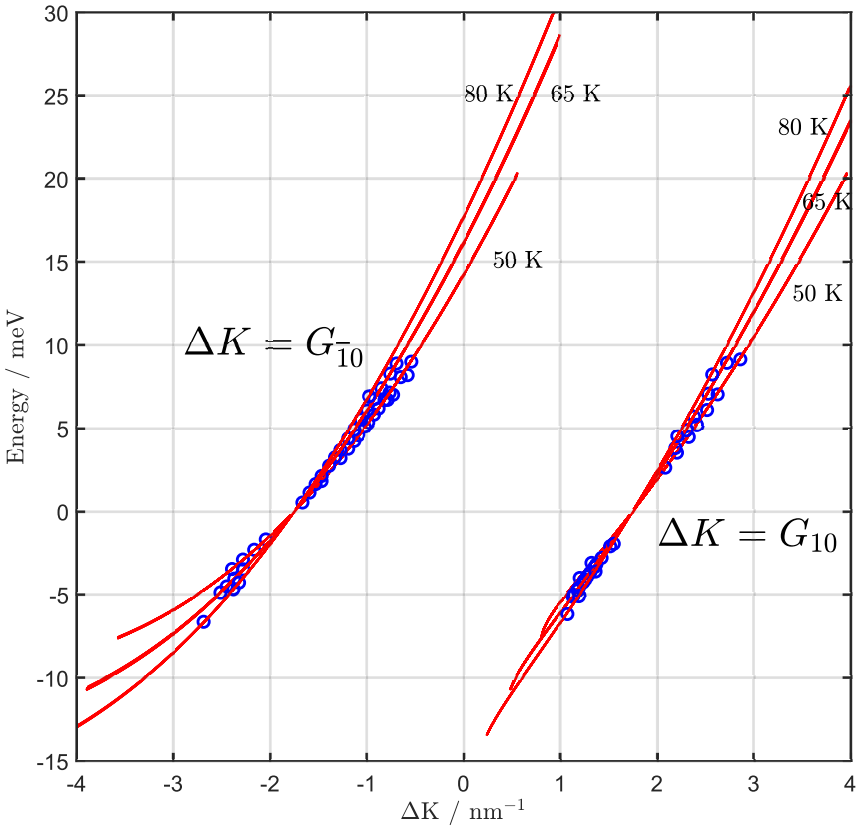

Figure 6.2: Plot of the calculated Decepton dispersion in red lines. The lines on the left represent a scattering vector in the $G_{\bar{1}0}$ direction and on the right G_{10}. The three separated lines originate from different nozzle temperatures (50 K, 65 K, 80 K) hence different helium beam energies. The blue circles represent the experimentally measured deceptons.

flight is shifted by[19]:

$$\Delta t_{TOF} = L_{CD}\left(\frac{1}{v_0} - \frac{1}{v^*}\right) \tag{6.2}$$

The peak in the TOF spectrum origins from the first order diffraction of helium atoms with a different velocity compared to the median velocity of the beam. If this peak is wrongly assigned to an inelastic feature a ΔE, ΔK pair is extracted from the TOF spectrum, similar to a real phonon event. Therefore in analogy to the surface phonon dispersion a "false" dispersion of deceptons can be defined. Since deceptons are only occurring due to diffraction they appear near the diffraction peaks and never in the vicinity of the specular peak[21].
Hence when looking at a TOF spectrum one has to look out for these deceptons and distinguish them from the actual phonons. In the surface phonon dispersion these peaks have to be identified and removed.

In figure 6.2 this pseudo decepton dispersion is drawn for the $\overline{\Gamma M}$ direction and nozzle temperatures of 50 K, 65 K and 80 K . To get this dispersion the transformation from the TOF-spectrum to ΔE and ΔK for every v^* is performed. ΔE is determined using equation 3.24 with the new flight time $t_{CD} = L_{CD}/v^*$. The correct scattering angle θ_i is given by the Bragg condition with the new k^* and the reciprocal lattice vector G_{hk} in the neighbourhood where the deceptons appear using equation 3.9. In the last step the parallel momentum transfer is calculated with equation 3.21 using the new values for θ_i and ΔE.
The three left lines include the $G_{\overline{1}0}$ scattering vector and on the right the scattering vector G_{10}. In figure 6.2 the experimentally measured peaks which are assigned to deceptons match the calculated decepton dispersion. During all TOF measurements a great amount of deceptons has been found which leads to the assumption that the velocity distribution of the produced helium beam is rather broad. When comparing this to the usual broadening $\Delta v/v \approx 0.01$ of the beam these velocity components must be from the outer wings of the velocity distribution. Textbooks find the origin in the vacuum chambers used in differential pumping systems[19]. The overall intensity of this component in the velocity distribution is extremely small. However, since we are dealing with an elastic scattering event, the scattered intensity becomes comparable to the scattered intensity of inelastic events from the mean velocity.

In figure 6.3(a) a TOF spectrum containing a decepton is shown. At an energy transfer of 1.5 meV the peak for the Rayleigh mode can be seen. The blue line in (b) intersects several calculated phonon modes at this value. When looking at the characteristic peak at -3.5 meV in (a) and at the corresponding y-value of the red scan curve in (b) no phonon mode is in the vicinity (green circle). Indeed, when checking with the decepton dispersion it is found that this peak corresponds to a decepton.

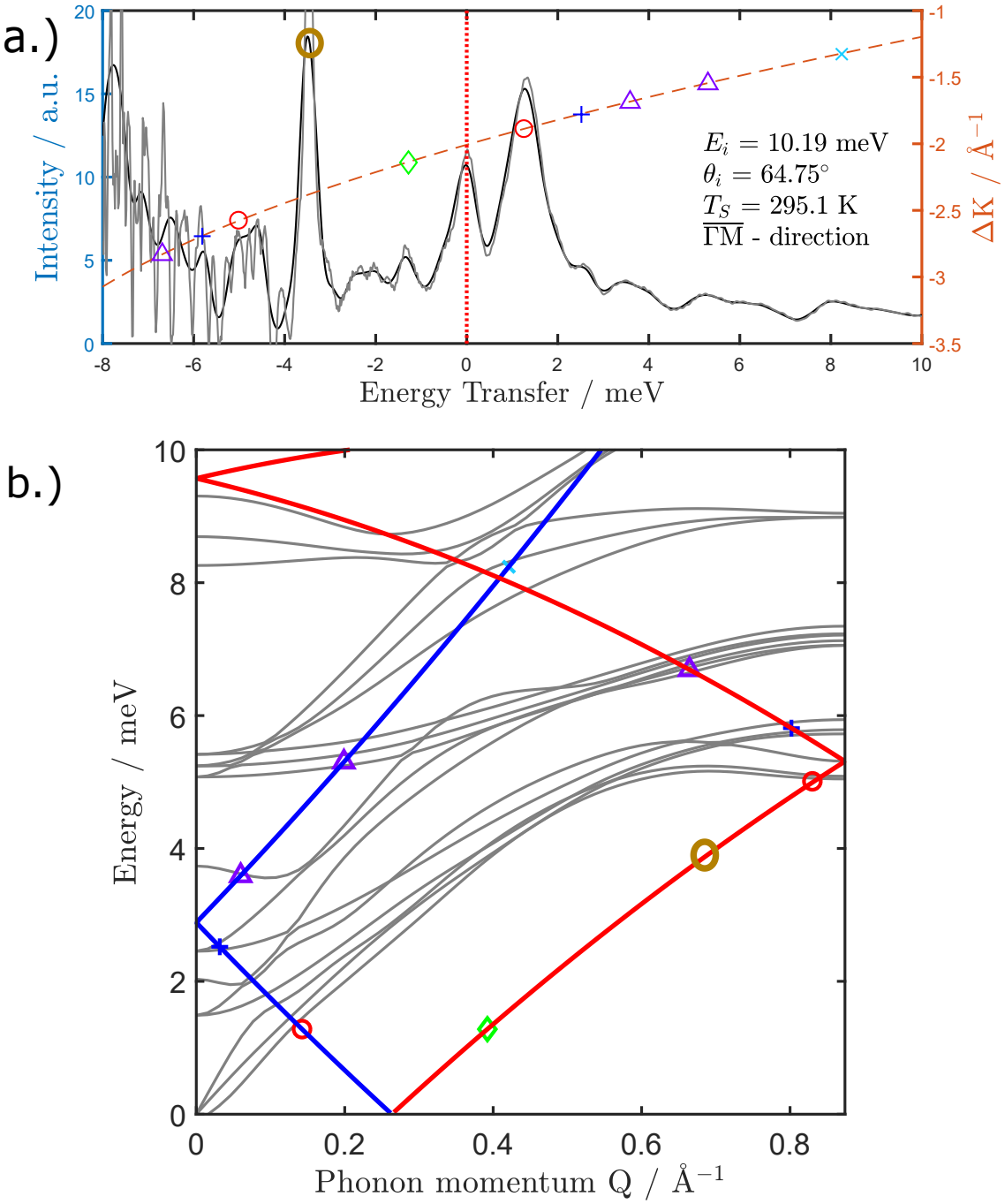

Figure 6.3: Illustration of a performed TOF measurement showing a decepton. In (a) the TOF spectrum is depicted. Besides the Rayleigh peak at around 1.5 meV a sharp decepton peak at −3.5 meV can be found. In (b) the corresponding scan curve is plotted with the theoretical calculation in the background. The brown circle marks the point of the decepton energy.

6.3 Complete Surface Phonon Dispersion

To get the complete surface phonon dispersion various TOF spectra have been measured with different incident angles and helium beam energies. By combining all spectra the measured surface phonon dispersion can be seen in figure 6.4.
In general phonon events were easier to identify in the $\overline{\Gamma M}$ direction compared to $\overline{\Gamma K}$.
All measurements in $\overline{\Gamma M}$ had better count rates and therefore higher energy phonons

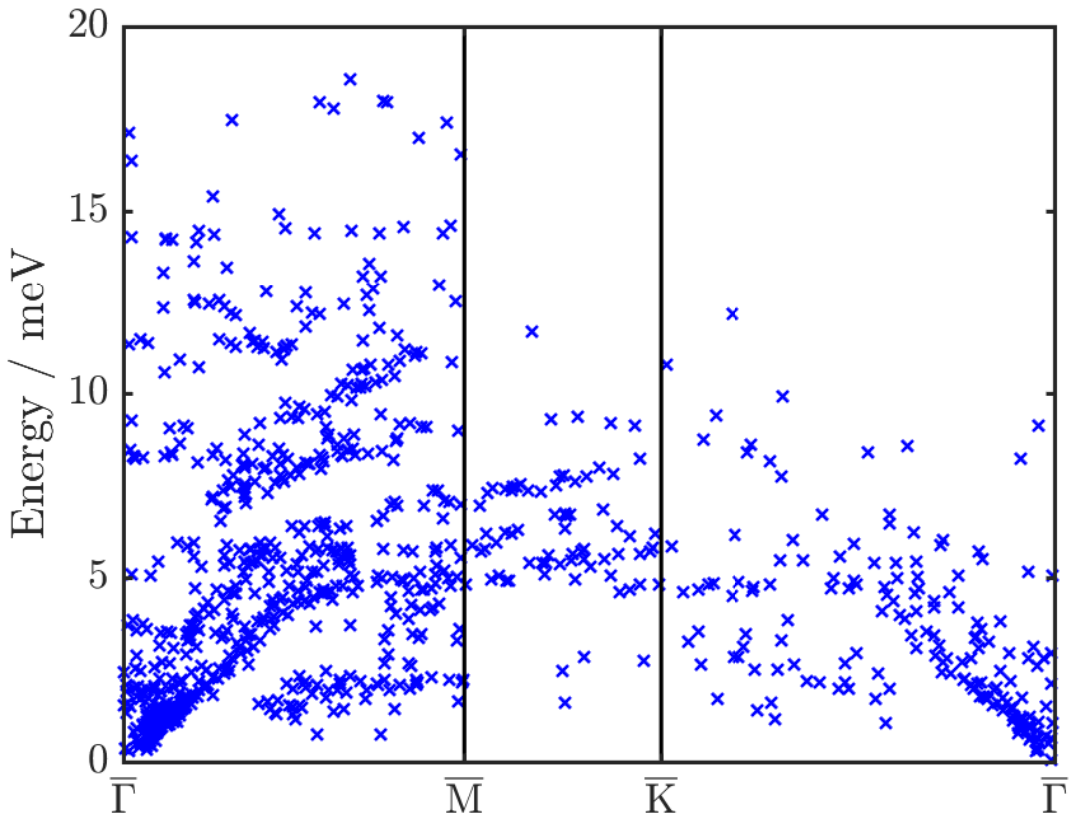

Figure 6.4: Plot of the measured surface phonon energies using many TOF-spectra at various incident angles, beam energies and sample temperatures.

were observable. The better signal in the $\overline{\Gamma M}$ direction may come from the difficult alignment of the sample in the main chamber. When orienting the sample in the $\overline{\Gamma K}$ orientation and at incident angles θ_i the sample holder shadows small parts of the sample. Secondly for $\overline{\Gamma K}$ the first order diffraction peaks are at higher incident angles. Hence, to cover the whole Brillouin zone the measurements had to be taken at larger angles. Due to the small counting rate at these angles the signal to noise ratio is rather small and it is difficult to identify peaks.
Phonons with energies higher than 17 meV are generally hard to detect with helium atom scattering, the reason being the difficult identification of significant peaks in the TOF

spectrum. On the creation side the signal oscillates too much to be able to distinguish between noise and significant peaks. On the annihilation side the signal becomes too flat to see any distinct peaks in the spectrum and the occupation of phonons (according to the Bose-Einstein distribution) decreases.
Additional effects such as kinematical focussing (see chapter 3.6.2) complicated the interpretation of TOF spectra.

6.3.1 Bulk Phonon Dispersion

In previous works the bulk phonon dispersion of Bi_2Se_3 has been theoretically calculated[47]. The calculations were performed using density functional theory with and without spin-orbit-coupling (SOC). The phonon dispersion is shown in figure 6.5(a).
Bi_2Se_3 has N=5 atoms in the primitive unit cell. Therefore in three dimensions the whole dispersion has 3N=15 modes with 3 acoustic and 3N-3=12 optic branches. In figure 6.5(a) the three acoustic modes start with zero frequency/energy at the Γ-Point. In general most phonon curves calculated with local density approximation (LDA) and SOC are a little lower than without including SOC. The two lowest branches show soft oscillating modes along Z-F and Γ-F. If SOC is included these soft modes transit to show imaginary phonon frequencies. This is an indication for dynamic unstabilities of the Bi_2Se_3 single crystal. The soft modes suggest weak interatomic bonding and a possible strong anharmonicity[47].
The symbols in the bulk phonon dispersion label the high symmetry points of the three dimensional Brillouin zone as can be seen in figure 6.5(b). Γ-Z has no influence on the surface dispersion since the projection onto the surface Brillouin zone is zero. The projected directions Γ-L and Γ-F are comparable to the surface direction $\overline{\Gamma}$-$\overline{\mathrm{M}}$.

6.3.2 Phonon group velocity at the surface

In the low energy region of the phonon dispersion the Rayleigh mode shows a linear behaviour. If the slope in this region is known the group velocity can be calculated. In figure 6.6 the Rayleigh mode is plotted and the lower energy regions are fitted with a first order polynomial. The following values have been calculated for the high symmetry directions $\overline{\Gamma\mathrm{M}}$ and $\overline{\Gamma\mathrm{K}}$:

$$k_{\overline{\Gamma\mathrm{M}}} = (10.3 \pm 0.3)\,\mathrm{meV\AA}, \qquad k_{\overline{\Gamma\mathrm{K}}} = (10.3 \pm 0.3)\,\mathrm{meV\AA}$$

To get the group velocity one has to divide by $\hbar$.

$$v_{\overline{\Gamma\mathrm{M}}} = (1557 \pm 43)\,\mathrm{m\,s^{-1}}, \qquad v_{\overline{\Gamma\mathrm{K}}} = (1564 \pm 44)\,\mathrm{m\,s^{-1}}$$

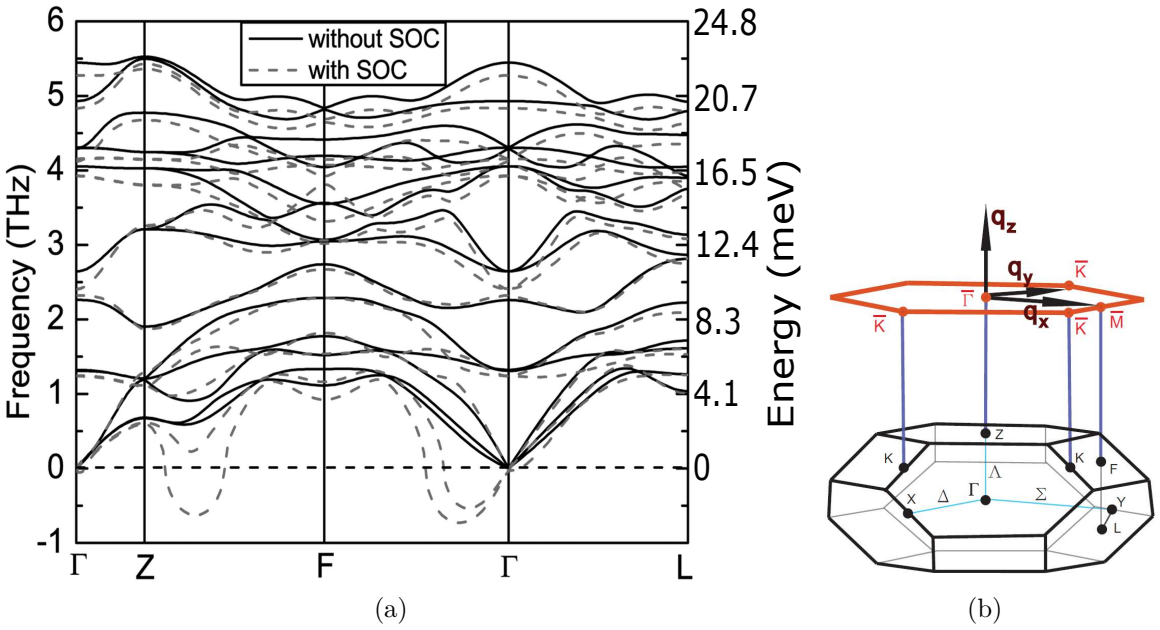

Figure 6.5: Plot of the calculated bulk phonon dispersion of Bi_2Se_3 (a) using density functional theory[47] with schematic view of the bulk three-dimensional Brillouin zone and the two dimensional Brillouin zone of the projected surface (b). From supplement[40]

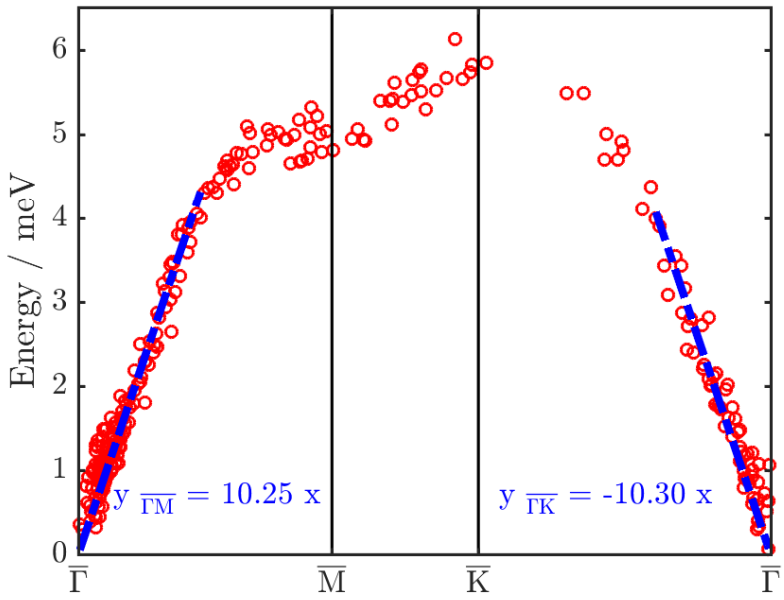

Figure 6.6: Graph of the Rayleigh mode with linear fit in both high symmetry directions. The slopes of the lower energy part of this mode corresponds to the group velocity of the phonons in the crystal.

For an elastic medium the group velocity at the surface can be calculated if the bulk modulus is well known[48]. In general the speed of surface acoustic waves is lower than the speed of the slowest bulk wave propagating in the same direction. To determine the speed of surface acoustic waves the following equation can be used as an approximation:

$$\xi = \frac{0.87 + 1.12\sigma}{1 + \sigma} \quad \text{with} \quad \sigma = \frac{1 - 2v_t^2/v_l^2}{2(1 - v_t^2/v_l^2)} \tag{6.3}$$

where v_l and $v_t (< v_l)$ are the speed of sound for longitudinal and transverse waves in the bulk medium. ξ is the ratio between the speed of the Rayleigh wave and the speed of transverse waves $\xi = v_{\mathbf{R}}/v_t$.
From literature[49] the speed of sound in Bi_2Se_3 are known to be $v_l \simeq 2900\,\mathrm{m\,s^{-1}}$ and $v_t \simeq 1700\,\mathrm{m\,s^{-1}}$. Inserting these values in the equations above and solving for $v_{\mathbf{R}}$ leads to a speed of the surface acoustic wave of

$$v_{\mathbf{R}} = 1561\,\mathrm{m\,s^{-1}}$$

This value is in good agreement with the above determined value from our measurements of the Rayleigh mode.

6.4 Comparison with theoretical calculations using DFPT

In the previous graphs of the scan curve theoretical calculations have been used to get an idea where the surface phonon modes could be located. For the calculation of these surface phonon dispersions density functional perturbation theory (DFPT) is used. The calculations were performed by Davide Campi (THEOS, EPFL Lausanne) using 3 quintuple layers without spin orbit coupling and without van der Waals forces between the individual quintuple layers. The calculations were done with the computational program *Quantum Espresso*[51].
For a precise calculation of the surface lattice vibrations, in principle spin-orbit corrections are necessary due to the heavy elements (Bi) in the compound as well as van der Waals (vdW) corrections which account for the bonds between the individual quintuple layers. However, for layered crystals with heavy elements, sometimes better agreement between the calculations and the experiment is found when ignoring both corrections instead of employing just one correction[6,52].
While SOC corrections typically soften the phonon modes, vdW forces make the lattice slightly more compact and stiffer so that both corrections compensate each other to some extent.
The results for Bi_2Se_3 can be seen in figure 6.7. The left column highlights the longitudinal polarizations (also see chapter 3.6.1) for the first (L1), second (L2), and third (L3) layer. The right column shows the shear vertical polarizations for the first three layers (SV1-SV3). The intensity of each mode on the corresponding layer is given by the colour code.

In figure 6.8 the experimental determined phonon energies are compared with the theoretical phonon dispersion. In general the experimentally measured phonon energies are in good agreement with the theoretical calculated dispersion. Phonons with energies up to 19 meV were detected which overlap with the calculations.
The different colours and symbols in figure 6.8 represent the various phonon modes. The assignment to different phonon modes is based on a comparison with calculations i.e if an experimental data point falls close to a calculated dispersion it is likely to belong to this mode. The red circles for the Rayleigh mode are very prominent. In the lower energy regime phonon modes (represented with green squares) are measured which are not seen in the calculations. They will be discussed in chapter 6.5.
In general more phonons were detected in the $\overline{\Gamma M}$ direction because of the better intensity and counting rates in the TOF spectra.

The measured surface phonon dispersion can now be compared to the bulk phonon

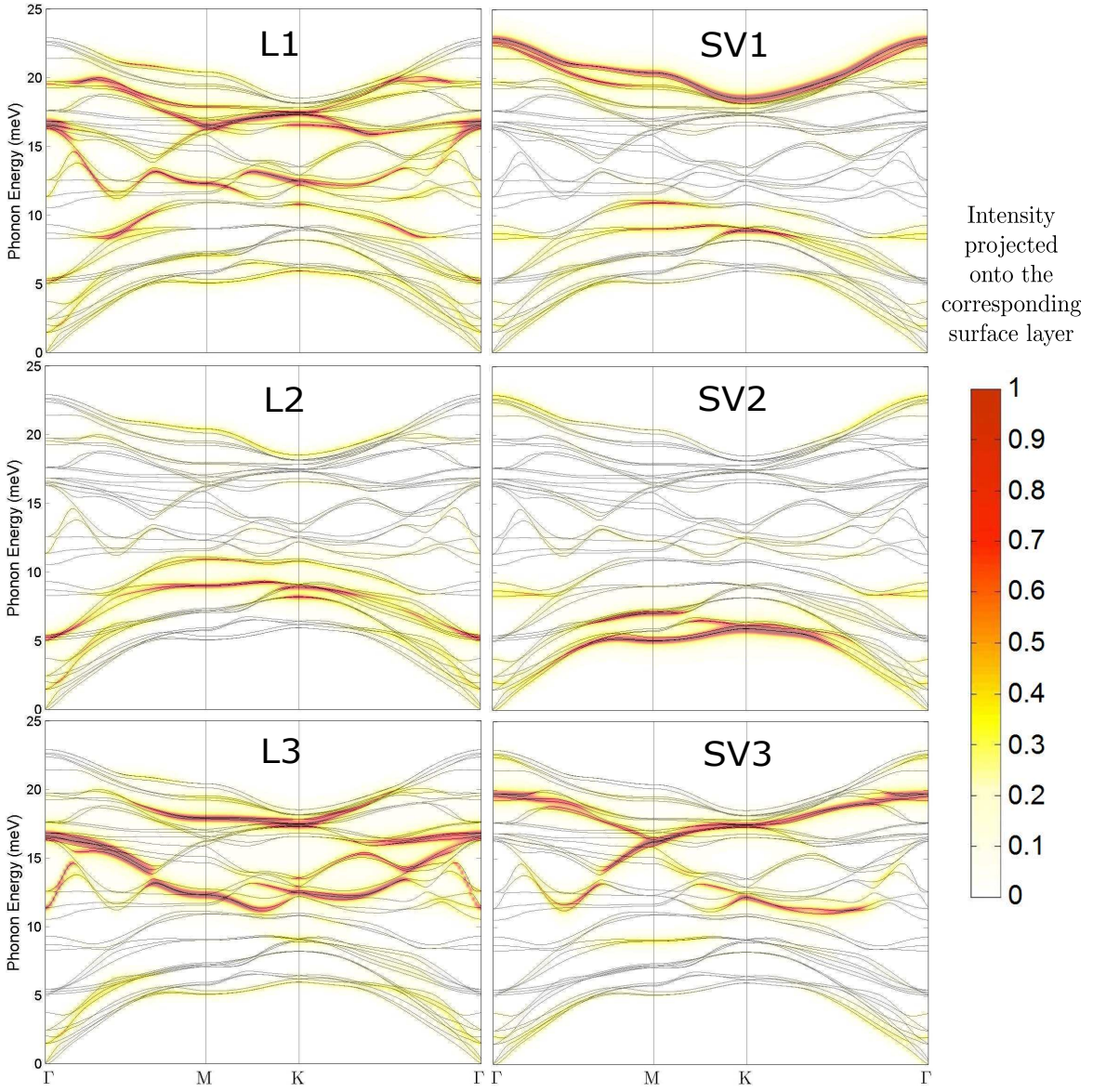

Figure 6.7: Illustration of the theoretical calculations of the surface phonon dispersion of Bi_2Se_3 using DFPT. The calculations were performed without spin orbit coupling for a quintuple layer by D. Campi[50]. In the left column the longitudinal polarizations for the first three layers are highlighted (L1-L3). The right column shows the shear vertical polarizations (SV1-SV3).

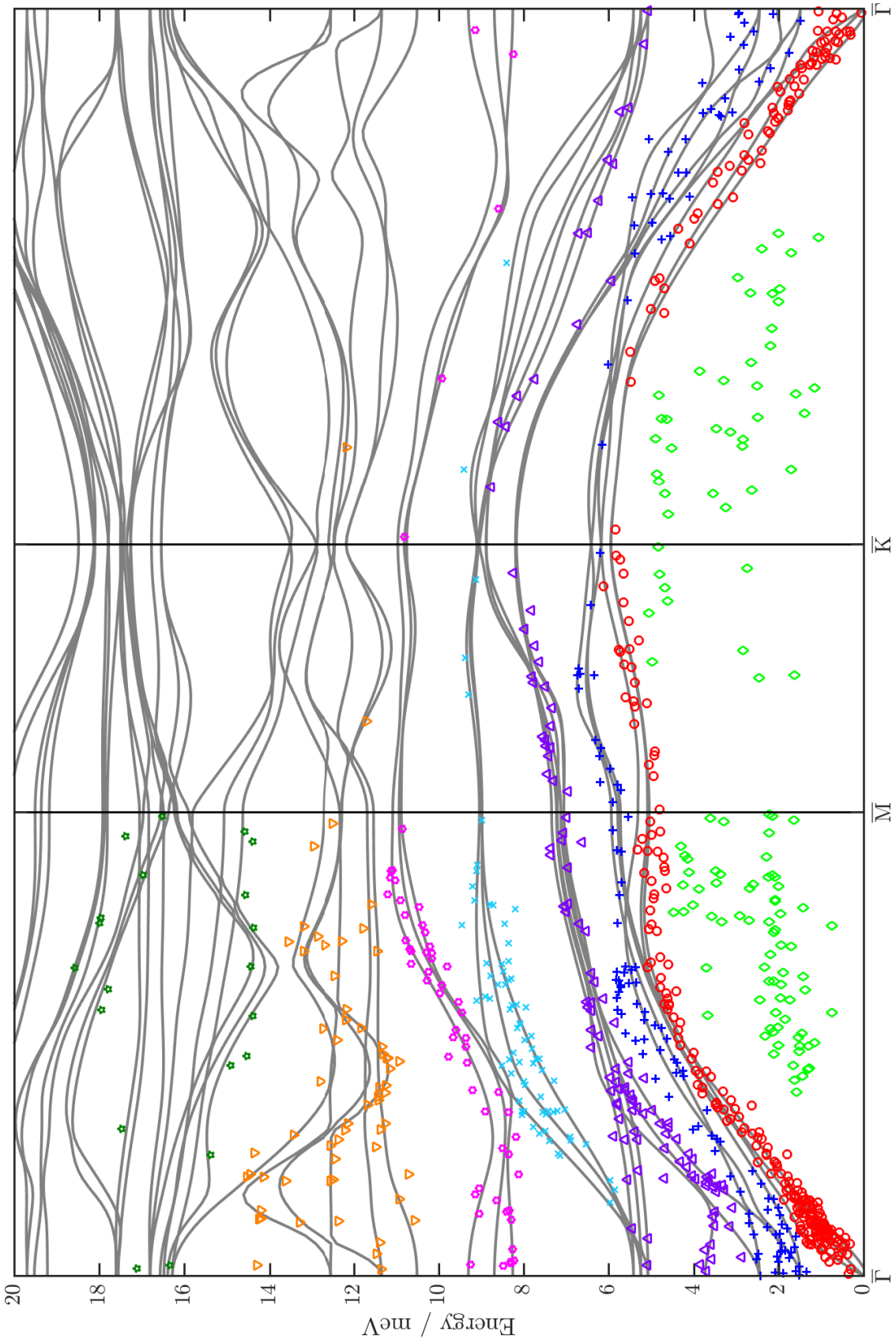

Figure 6.8: Plot of the complete surface phonon dispersion of Bi_2Se_3. All markers origin from TOF measurements. Different colours represent different modes. The grey lines were calculated with DFPT.

dispersion.
The energy of the Rayleigh mode in figure 6.8 is a bit lower than the lowest mode of the bulk dispersion in figure 6.5(a). This is explained due to the weaker bonding of the atoms at the surface. The spring constant at the surface is lower and therefore also the energy of the phonons is decreased. The maximum optical phonon energies of about 20 meV are the same for both dispersions.
Considering the fact that the Γ-L and Γ-F direction projected on the surface gives the $\overline{\Gamma M}$ direction, the dispersion curves should be similar albeit slightly lower in energy on the surface. (see figure 6.5(b)) The lowest mode of the bulk dispersion in the Γ-F direction starts at zero with a linear behaviour and hits the Brillouin zone boundary at an energy of 5 meV. The same behaviour can be seen in the Rayleigh mode in the $\overline{\Gamma M}$ direction of the surface dispersion.

There is no general formula for the number of acoustic and optical modes in a surface phonon dispersion. When looking at the energies of the lowest modes in figure 6.8 and comparing them to the bulk acoustic modes it appears as if there are three acoustic branches in the surface phonon dispersion. First the Rayleigh mode and then two additional modes. The mode above the Rayleigh mode is usually called longitudinal resonance in metallic surfaces. The modes split up into three individual bands due to the number of layers in the calculation.

When comparing figure 6.8 with figure 6.7 one can see that the taken measurements mainly created/annihilated phonons in the first two layers of the sample. Especially the phonons of the second layer (L2, SV2) were very prominent in the TOF-spectra since their phonons modes are in the lower energy parts of the dispersion. But one has to keep in mind that the lower energy phonons are easier to measure with our measurement technique. Due to the weak electron-phonon coupling it is hard to observe subsurface modes.
When looking at the polarization of the measured phonons the longitudinal modes of the first two layers (L1, L2) are mostly seen in the measurements. Also the shear vertical mode of the second layer (SV2) is eminent in the TOF data since this mode contains the Rayleigh mode which is very significant in our measurements.

To get a better impression how the whole surface phonon dispersion evolves, various representative TOF-spectra are described on the following pages.

In figure 6.9 three TOF-spectra are depicted. In these graphs the signal transformed to energy scale is shown together with the actual momentum transfer of the phonon given by the scan curve. Each peak which has been identified as a phonon event in the TOF signal is indicated by a symbol plotted onto the scancurve to determine the correct

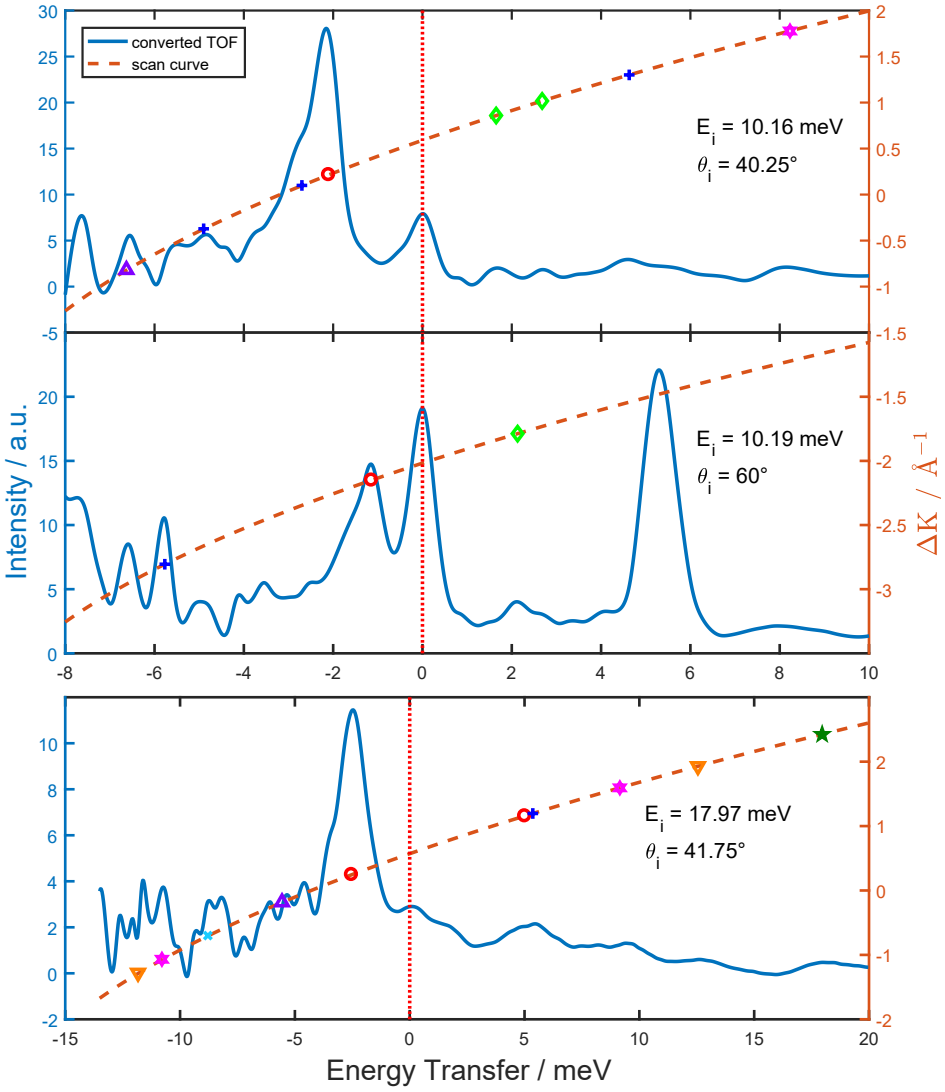

Figure 6.9: Comparison of different TOF spectra in the $\overline{\Gamma M}$ direction with various incident Energies E_i and angles θ_i. For the two upper graphs the nozzle temperatures was set to 50 K, and for the bottom one to 80 K which lead to the respective incident energies. The sample was held at room temperature.

momentum transfer. For better identification the symbols are the same ones used for the entire surface phonon dispersion (figure 6.8).
In the first graph of figure 6.9 a well defined peak corresponding to the Rayleigh mode (red circle) can be seen along with other smaller peaks. The interesting part are the two peaks at around 3 meV indicated with green squares. These phonon modes are visible in the experimental data, even though there is no indication of theses modes in the DFPT-simulations (see chapter 6.5). The momentum transfer in this first plot varies from -0.8 to $1.7\,\text{Å}^{-1}$.
In the second plot once again a distinct Rayleigh peak arises along with an unpredicted low mode peak. The peak at 5.5 meV derives from a decepton and is therefore omitted in the phonon dispersion. The momentum transfer of the created/annihilated phonons ranges from -2.6 to $-1.7\,\text{Å}^{-1}$.
In the third graph the nozzle temperature was set to 80 K which leads according to equation 2.3 to a much higher incident energy of $E_i = 17.97$ meV. This range of energy tends to result in a bigger amount of creation/annihilation of phonons, as can be seen by the number of peaks. Therefore more symbols appear on the scan curve. However the overall intensity compared to the two upper graphs is much lower, which makes the distinction between significant peaks and background noise even more difficult. With this beam energy phonons with higher energy transfer such as 18 meV (green star) and therefore optical modes can be observed.
In further examples the effect of changing the sample temperature is illustrated. Figure 6.10 compares three different TOF spectra in the high symmetry direction $\overline{\Gamma\text{K}}$ with various incident Energies E_i, angles θ_i and sample temperatures T_S.
In figure 6.10 the uppermost graph depicts a converted TOF spectrum with a sample temperature of $T_S = 123.1$ K. The sample was cooled using liquid nitrogen. Apart from the strong Rayleigh mode peak only very few phonon modes are observed. Directly below a comparable spectrum with similar beam energy and incident angle but with the sample at room temperature is depicted. Compared to this plot the overall intensity of the cooled sample is lower. Therefore the low sample temperature has a big impact on the yield of inelasticly scattered helium atoms. Phonons are less likely to be annihilated due to the occupation based on the Bose-Einstein distribution. However the probability for the creation of phonons at lower temperatures stays the same.
In the third graph of figure 6.10 a TOF spectrum with a very steep incident angle of $\theta_i = 13.45°$ is drawn. Typically the TOF spectra are taken in between the specular peak and the first order diffraction peak. In this plot, however, the spectrum was measured between the first and second order diffraction peak. In this graph only very few distinct peaks appear. This might be an effect deriving from the pseudo random technique. The smaller peaks can hardly be distinguished from the background noise after the deconvolution. (see chapter 3.6.2)
Apart from two peaks based on the Rayleigh mode only two other modes can be observed.

At an energy of $-2\,\mathrm{meV}$ a decepton peak appears. The intensity of the diffuse elastic peak is high because the measurement was taken near the first order elastic peak.

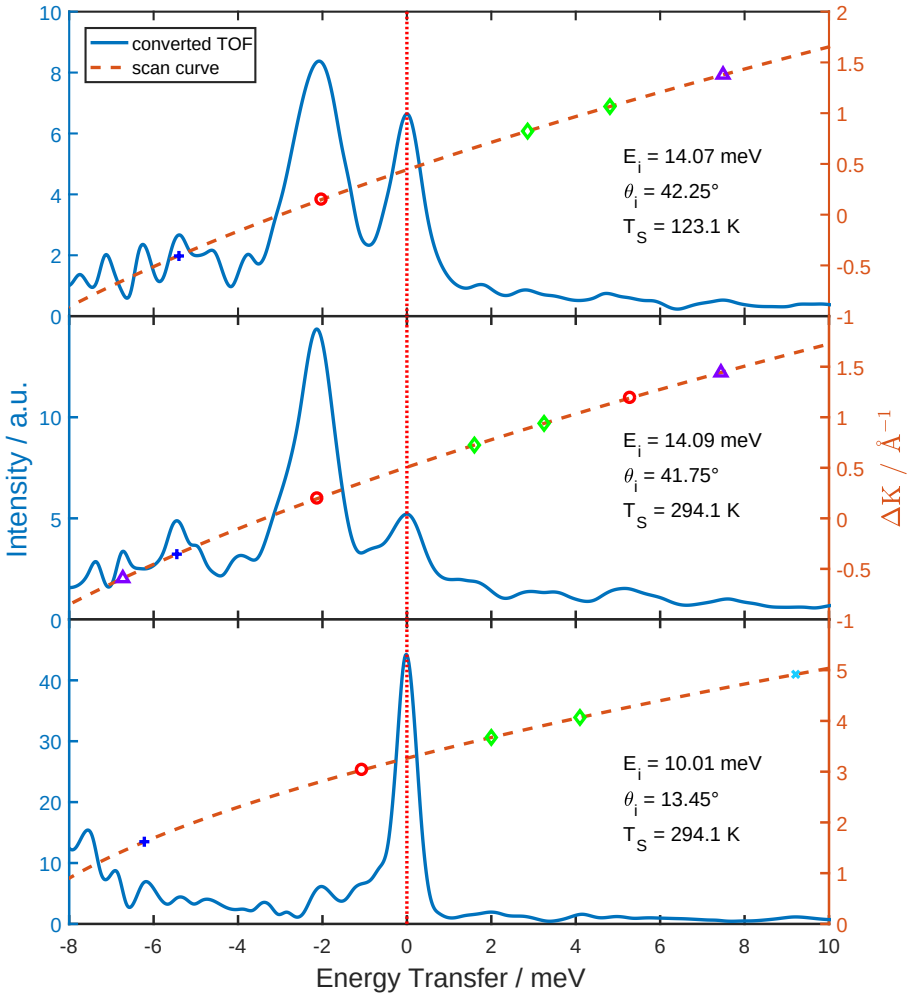

Figure 6.10: Comparison of different TOF spectra in the $\overline{\Gamma\mathrm{K}}$ direction with various incident Energies E_i, angles θ_i and sample temperatures T_S. In the first graph the sample was cooled down to $T_S = 123.1\,\mathrm{K}$. The bottom spectrum was measured near the first order elastic peak.

A good comparison between the intensity in the two high symmetry directions $\overline{\Gamma\mathrm{M}}$ and $\overline{\Gamma\mathrm{K}}$ is given in figure 6.11 and the top graph in figure 6.9. In comparison the spectrum in the $\overline{\Gamma\mathrm{K}}$ direction shows fewer peaks than the $\overline{\Gamma\mathrm{M}}$ spectrum. This behaviour was observed several times when comparing the high symmetry direction. A possible reason might be the difficult alignment of the sample for different azimuthal orientations.

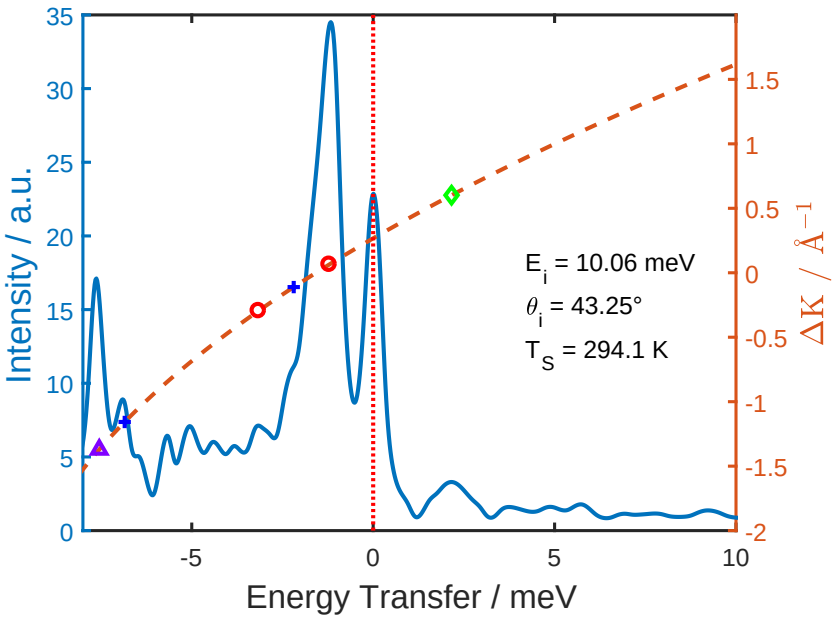

Figure 6.11: Plot of a TOF spectrum which shows a distinct peak for an unpredicted low mode.

6.5 Unpredicted low modes

During the analysis of the TOF spectra phonon energies have been identified which are not found in the DFPT simulations. These modes are energetically lower than the Rayleigh mode. Therefore they are called low modes. Figure 6.11 shows one of these low modes. In this spectrum a strong indication for a lower lying mode is given at around 2 meV. The origin of the low modes could be due to collective charge density oscillations as described below.

Elementary excitations of large-period surface charge density waves, so-called phasons and amplitudons, have been observed with optical pump-probe techniques in cuprate superconductors[53,54].

HAS has also been considered for a possible detection of additional dispersion curves besides those of surface phonons. Although helium atoms at thermal energies are scattered off a conducting solid surface at distances as large as 0.3 nm from the first atomic layer, where the electronic density is of the order of 10^{-4} a.u., helium atom scattering has proven to be sensitive to dynamic charge density oscillations which are two orders of magnitude smaller[55]. In this way surface and subsurface phonons can be detected via the tiny phonon-induced modulation of the surface charge density, and the corresponding mode-selected electron-phonon coupling can be directly measured[6,56].

Here the question arises whether elementary-excitations of the surface charge density itself can be measured as well. Indeed elementary excitations of large-period surface charge density waves (CDW), have been observed with HAS for the reconstructed Au(111) sur-

face[57,58] and probably also in graphene/Ru(0001)[59].
Since the band structure at the Fermi level of semi-metal surfaces like those of Bi(111) and Sb(111) is characterized by arrays of narrow electron and hole pockets in the reciprocal space, static long-period charge density oscillations are expected in real space. There has been a debate about whether CDWs can exist in Bi(111) and Sb(111)[60,61]. On the other hand the spin-orbit coupling, which makes Sb(111) a weak topological insulator with spin-split bands around the zone centre[62,63], can in principle support a spin-density wave (SDW). Indeed conventional inelastic HAS measurements on Sb(111) revealed two additional branches below the usual Rayleigh wave (RW) branch[64]. The comparison with previous DFPT calculations of the surface phonon dispersion curves of both Sb(111)[63] and Bi(111)[6] shows that the two low-energy branches cannot be attributed to any possible phonon branch of the clean surface, and were therefore assigned to a phason-amplitudon pair[41].
It seems quite likely that a similar phenomenon can be observed on Bi_2Se_3(111) with its complicated electronic structure at the Fermi level. Here the evolution of multiple 2DEG (2D electron gas) states after cleaving[41] (figure 4.3), due to the adsorption of residual gas atoms, makes this connection possible. Nevertheless a distinct assignment of these modes to phason-amplitudon pairs remains pending and would be beyond the scope of this work.

6.6 Kohn anomaly

Previous to this work the group of Zhu *et al.* has performed measurements of the surface phonon dispersion of Bi_2Se_3 (111)[40]. The results show an indication of a strong Kohn Anomaly.

Such an anomaly can appear in a phonon branch of a metal. For a specific wave vector, the frequency of a phonon is significantly lowered, and therefore a discontinuity in the derivative of the dispersion arises. This discontinuity is produced by a sudden change in the screening of lattice vibrations by conduction electrons. The energy necessary for electron-hole excitations across the Fermi-surface is provided by phonons via the electron-phonon coupling. This energy is subtracted from the phonon energy. In extreme cases this may lead to phonon energies of 0 meV. In figure 6.12 the possible transitions for creating an electron-hole pair are shown. If the electron hops from one side to the other a Kohn anomaly may appear. This effect is only possible for vectors that are nesting vectors of the Fermi surface. This vector is $2k_F$, with k_F being the Fermi wave vector.
The measurements by Zhu *et al.* have also been performed with helium atom scattering using a different helium atom detection.

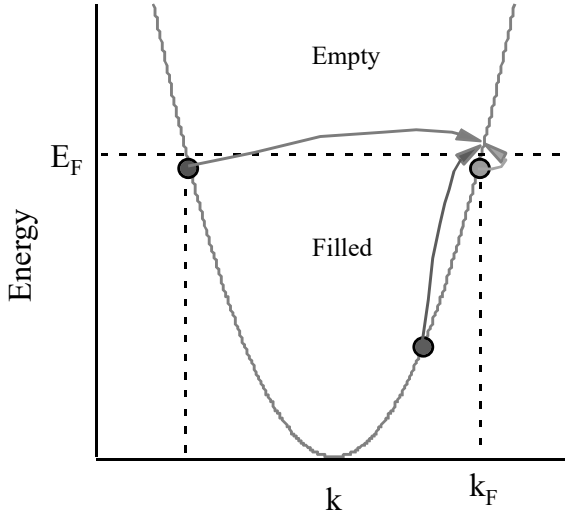

Figure 6.12: Illustration of a simple free electron band structure showing the possible transitions creating electron-hole pairs[65].

In contradiction to the measurements in Graz Zhu *et al.* observed a strong Kohn anomaly. In Figure 6.13 the orange dots represent the experimental data, while the calculated dispersion curves are represented by black dots. For the theoretical calculation a pseudo charge model[66] was used and applied to slab geometries containing 30 quintuples layers. The gray background of the graph represents the projection of the bulk bands on the surface Brillouin zone.
At a wave vector of around $0.25\,\text{Å}^{-1}$ the Kohn anomaly becomes visible.
In our measurements there was no indication of such a Kohn anomaly at all. The theoretical simulations using DFPT done by D. Campi[50] can not reproduce a Kohn anomaly because it is a non-adiabatic process. In addition we always saw very strong Rayleigh modes in all performed TOF measurements as can be seen in the amount of red circles in figure 6.8, which were claimed to be absent in previous works by Zhu *et al.*[40].
A possible explanation could be the quality of the sample and a lower resolution of the experimental setup used by Zhu *et al.* When comparing their elastic spectra with our measurements Zhu *et al* had very broad diffuse elastic peaks. In particular in the long wavelength limit (close to Γ), ΔE is very small for the Rayleigh mode. Hence it might be difficult to distinguish a Rayleigh mode from the diffuse elastic peak.
Since the sample is not the exact same their Bi_2Se_3 might have had too many steps at the surface. This would lead to their broad diffraction peaks compared to our results (see figure 5.2).
A Kohn anomaly becomes typically more pronounced at lower temperatures. However even our measurements with the sample cooled to 123 K showed no indent in the lowest phonon branch.

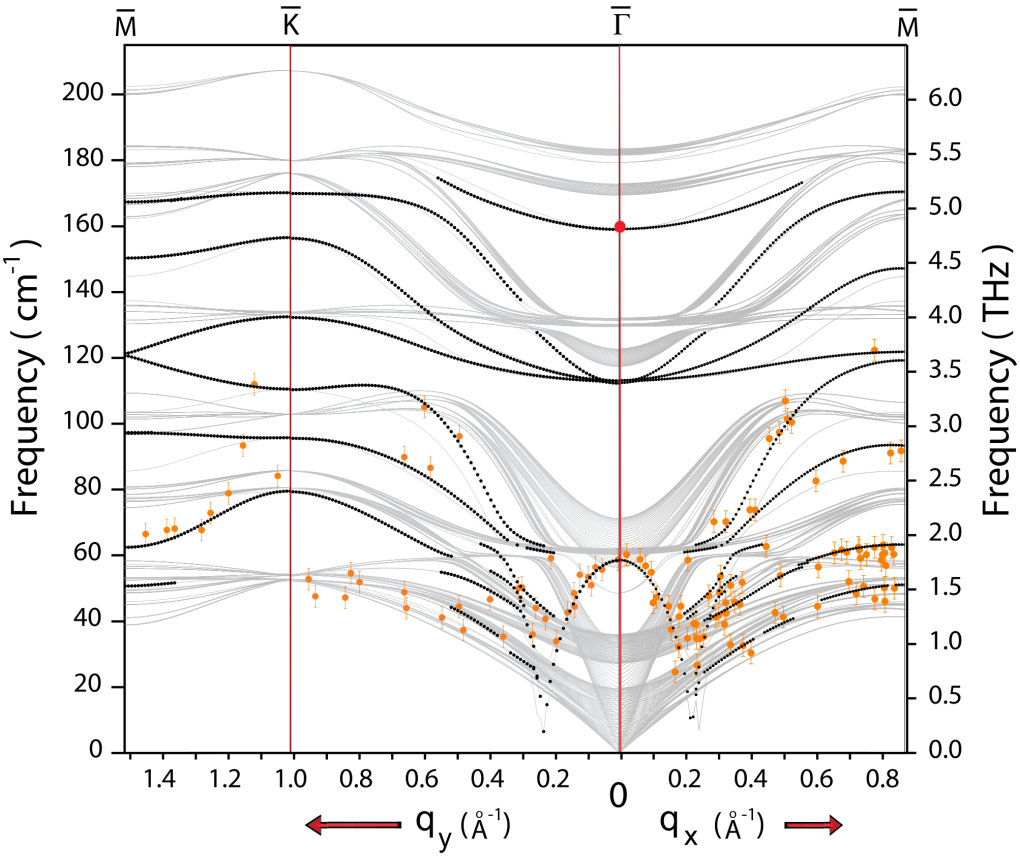

Figure 6.13: Surface phonon dispersion of Bi_2Se_3 along $\overline{\Gamma K}$ and $\overline{\Gamma M}$ as measured by Zhu *et al*[40]. Experimental data appear as orange dots while the calculated dispersion curves, using a pseudo charge model[66] are represented by black dots. The gray background represents the projection of the bulk bands on the surface Brillouin zone.

The exact reason for our measurements not showing any indications of a Kohn anomaly is yet unsolved and needs further investigation.

7 Summary

In the course of this work the surface dynamics of Bi_2Se_3 have been investigated using elastic and inelastic helium atom scattering. After the sample preparation and a first characterization of the material the lattice constant was determined to be $a = (4.14 \pm 0.01)$ Å. Performing various elastic measurements at various sample temperatures lead to a surface Debye temperature of $\theta_D = (114 \pm 6)$ K.
The main focus of the work were the surface lattice vibrations of the Bi_2Se_3 surface investigated by time of flight-spectroscopy. Many TOF-spectra have been collected to obtain the surface phonon energies. Using various incident angels, beam energies and sample temperatures the entire surface phonon dispersion was extracted.
From the lowest mode (Rayleigh mode) the speed of surface acoustic waves in this material was determined to be $v_g = (1560 \pm 44)\,\mathrm{m\,s^{-1}}$, which is in good agreement with predictions from elastic medium theory.
Interestingly the Rayleigh mode is the most prominent feature in the TOF-spectra even though it was claimed to be absent by Zhu *et al*[40]. The measured results of the dispersion were compared with theoretical density functional perturbation theory calculations. A good agreement was found except for unpredicted low modes below the Rayleigh mode. The origin of these low modes could be due to collective charge density oscillations.
The determined surface phonon dispersion was also compared with the respective bulk dispersion as well as other existing works. The work of one previous group[40] has shown indications of a strong Kohn anomaly which has not been seen in our measurements. Disparities in the experimental setup or the sample itself may be the cause of this discrepancy.

Danksagung

An dieser Stelle möchte ich mich bei all den Menschen bedanken, die mich während meiner gesamten Studienzeit und insbesondere bei der Ausarbeitung dieser Masterarbeit unterstützt und motiviert haben.
Auf dieser Reise habe ich viele neue Freunde gewonnen, mit deren Hilfe und Beistand ich meinen persönlichen Weg finden konnte. Die wechselseitige Impulsgebung trug maßgeblich zu meinem Erfolg bei und die gemeinsamen außeruniversitären Erlebnisse möchte ich niemals missen.

Mein besonderer Dank gebührt Herrn Univ.-Prof. Dr. Wolfgang Ernst, der meine Masterarbeit durch seine fachliche Kompetenz und langjährige Erfahrung entscheidend unterstützt und begleitet hat. Für die hilfreichen Anregungen und die konstruktive Kritik möchte ich mich herzlich bedanken.

Ebenfalls möchte ich Herrn Dr. Toni Tamtögl meinen Dank aussprechen. Immer stand er mir mit seinem Rat fördernd zur Seite, half mir über schwierige Themen hinweg und gab mir durch kritisches Hinterfragen neue Denkanstöße. Ich danke ihm aufs herzlichste für sein Interesse, seine Hilfsbereitschaft und das Korrekturlesen dieser Arbeit. Nicht nur im Labor und bei zahlreichen interessanten Debatten befanden wir uns auf derselben Wellenlänge, auch abseits der Physik kam der Spaß nie zu kurz.

Außerdem freute es mich sehr, so nett am Institut für Experimentalphysik aufgenommen worden zu sein. Danke an Patrick für die erste Einführung und an Michael für die Unterstützung beim Programmieren. Ebenso haben alle anderen Kollegen zu dieser unvergesslichen Zeit am Institut beigetragen. Unsere gemeinsamen Mittagessen bei Toast und Nudeln haben mittlerweile Kultstatus erreicht.

Ein weiterer wichtiger Faktor während dieser Arbeit war mein zweites Standbein: die Musik. Als leidenschaftlicher Sänger und Gitarrist konnte ich beim Musizieren immer wieder neue Energie schöpfen.

Erwähnen möchte ich hier auch jenen Menschen der Impulsgeber für mein Studium war. Frau Mag. Christine Fest weckte in mir die Leidenschaft für die Physik.

Abschließend möchte ich mich bei meiner Familie, ganz speziell meinen Eltern Walter und Liane bedanken. Sie haben mir mein Studium nicht nur finanziell ermöglicht, sondern sind mir stets bei allen Herausforderungen hilfreich und beratend zur Seite gestanden. Danke für den starken emotionalen Rückhalt in den vergangenen Jahren.

Adrian Ruckhofer, Graz, 12.05.2017

8 Bibliography

[1] N. Balak. Charakterisierung, Aufbau und Steuerung einer Ultrahochvakuum Atomstrahlanlage. Master's thesis, Graz University of Technology, 2009.

[2] A. Tamtögl. *Surface Dynamics and Structure of Bi(111) from Helium Atom Scattering*. PhD thesis, Graz University of Technology, 2012.

[3] M. Mayrhofer-Reinhartshuber. Helium Atom Scattering from Surfaces including the Pseudo Random Chopper Technique. Master's thesis, Graz University of Technology, 2010.

[4] A. Tamtögl, M. Mayrhofer-Reinhartshuber, N. Balak, W. E. Ernst, and K. H. Rieder. Elastic and inelastic scattering of He atoms from Bi(111). *J. Phys.-Cond. Mat.*, 22:1–6, 2010.

[5] M. Mayrhofer-Reinhartshuber, A. Tamtögl, P. Kraus, K. H. Rieder, and W. E. Ernst. Vibrational dynamics and surface structure of Bi(111) from helium atom scattering measurements. *J. Phys.-Cond. Mat.*, 24:035410, 2012.

[6] Anton Tamtögl, Patrick Kraus, Michael Mayrhofer-Reinhartshuber, Davide Campi, Marco Bernasconi, Giorgio Benedek, and Wolfgang E. Ernst. Surface and subsurface phonons of Bi(111) measured with helium atom scattering. *Phys. Rev. B*, 87:035410, Jan 2013.

[7] P. Kraus, A. Tamtögl, M. Mayrhofer-Reinhartshuber, G. Benedek, and W. E. Ernst. Resonance-enhanced inelastic He-atom scattering from subsurface optical phonons of Bi(111). *Phys. Rev. B*, 87:245433, Jun 2013.

[8] A. Tamtögl, M. Mayrhofer-Reinhartshuber, P. Kraus, and W. E. Ernst. Surface Debye temperature and vibrational dynamics of Antimony(111) from helium atom scattering measurements. *Surf. Sci.*, 617(0):225 – 228, 2013.

[9] M. Mayrhofer-Reinhartshuber, A. Tamtögl, P. Kraus, and W. E. Ernst. Helium atom scattering investigation of the Sb(111) surface. *J. Phys.: Condens. Matter*, 25(39):395002, 2013.

[10] M. Mayrhofer-Reinhartshuber, P. Kraus, A. Tamtögl, S. Miret-Artés, and W. E. Ernst. Helium-surface interaction potential of Sb(111) from scattering experiments and close-coupling calculations. *Phys. Rev. B*, 88:205425, Nov 2013.

[11] P. Kraus, M. Mayrhofer-Reinhartshuber, Ch. Gösweiner, F. Apolloner, S. Miret-Artés, and W. E. Ernst. A Comparative Study of the He-Sb(111) Interaction Potential from Close-Coupling Calculations and Helium Atom Scattering Experiments. *Surf. Sci.*, 2014.

[12] D. R. Miller. *Atomic and Molecular Beam Methods*, volume 1. Oxford University Press, 1983.

[13] T. Reisinger, G. Bracco, S. Rehbein, G. Schmahl, W. E. Ernst, and B. Holst. Direct Images of the Virtual Source in a Supersonic Expansion. *J. Phys. Chem. A*, 111(111):12620, 2007.

[14] Ch. Kittel. *Introduction to Solid State Physics*. John Wiley & Sons Inc, 2005.

[15] H. Pauly. *Atom, Molecule, and Cluster Beams I.* 2000.

[16] C. V. Nowikow and R. Grice. Cross-correlation time-of-flight analysis of molecular beam scattering. *J. Phys. E*, 12(6), 1979.

[17] Sanford A. Safron. High-resolution helium atom scattering as a probe of surface vibrations. pages 129–212. John Wiley & Sons, Inc., 2007.

[18] Giorgio Benedek and J.Peter Toennies. Helium atom scattering spectroscopy of surface phonons: genesis and achievements. *Surf. Sci.*, 299:587 – 611, 1994.

[19] J. P. Toennies. *Surface Phonons*, volume 21. Springer, 1991.

[20] P. Kraus. Measurements of the He-Bi(111)) interaction potential using elastic helium atom scattering. Master's thesis, Graz University of Technology, 2011.

[21] R. B. Doak. *Single-Phonon Inelastic Scattering*, volume 2. Oxford University Press, 1983.

[22] G. Benedek, G. Brusdeylins, R. Bruce Doak, J. G. Skofronick, and J. Peter Toennies. Measurement of the Rayleigh surface-phonon dispersion curve for NaCl(001) from high-resolution He time-of-flight spectroscopy and from kinematical focusing angles. *Phys. Rev. B*, 28:2104–2113, Aug 1983.

[23] D. Farias and K. H. Rieder. Atomic beam diffraction from solid surfaces. *Rep. Prog. Phys.*, 61(12):1575, 1998.

[24] M. Z. Hasan and C. L. Kane. Colloquium. *Rev. Mod. Phys.*, 82:3045–3067, Nov 2010.

[25] Joel Moore. Topological insulators: The next generation. *Nat. Phys.*, 5(6):378–380, 2009.

[26] Laurens Molenkamp Marcel Franz. *Topological Insulators*, volume 6. Elsevier, 2013.

[27] Shun-Qing Shen. *Topological Insulators: Dirac Equation in Condensed Matters*. Springer Series in Solid-State Sciences. Springer, 2013 edition, 2013.

[28] Hailin Peng, Wenhui Dang, Jie Cao, Yulin Chen, Di Wu, Wenshan Zheng, Hui Li, Zhi-Xun Shen, and Zhongfan Liu. Topological insulator nanostructures for near-infrared transparent flexible electrodes. *Nat. Chem.*, 4(4):281–286, April 2012.

[29] Rama Venkatasubramanian, Edward Siivola, Thomas Colpitts, and Brooks O'Quinn. Thin-film thermoelectric devices with high room-temperature figures of merit. *Nature*, 413(6856):597–602, October 2001.

[30] Richard C. Hatch, Marco Bianchi, Dandan Guan, Shining Bao, Jianli Mi, Bo Brummerstedt Iversen, Louis Nilsson, Liv Hornekær, and Philip Hofmann. Stability of the Bi_2Se_3(111) topological state: Electron-phonon and electron-defect scattering. *Phys. Rev. B*, 83:241303, 2011.

[31] Z.-H. Pan, A. V. Fedorov, D. Gardner, Y. S. Lee, S. Chu, and T. Valla. Measurement of an Exceptionally Weak Electron-Phonon Coupling on the Surface of the Topological Insulator Bi_2Se_3 Using Angle-Resolved Photoemission Spectroscopy. *Phys. Rev. Lett.*, 108:187001, 2012.

[32] Chaoyu Chen, Zhuojin Xie, Ya Feng, Hemian Yi, Aiji Liang, Shaolong He, Daixiang Mou, Junfeng He, Yingying Peng, Xu Liu, et al. Tunable Dirac fermion dynamics in topological insulators. *Sci. Rep.*, 3:2411, 2013.

[33] Takeshi Kondo, Y. Nakashima, Y. Ota, Y. Ishida, W. Malaeb, K. Okazaki, S. Shin, M. Kriener, Satoshi Sasaki, Kouji Segawa, and Yoichi Ando. Anomalous Dressing of Dirac Fermions in the Topological Surface State of Bi_2Se_3, Bi_2Te_3, and Cu-Doped Bi_2Se_3. *Phys. Rev. Lett.*, 110:217601, May 2013.

[34] X. Zhu, L. Santos, C. Howard, R. Sankar, F. C. Chou, C. Chamon, and M. El-Batanouny. Electron-Phonon Coupling on the Surface of the Topological Insulator Bi_2Se_3 Determined from Surface-Phonon Dispersion Measurements. *Phys. Rev. Lett.*, 108:185501, 2012.

[35] Sébastien Giraud, Arijit Kundu, and Reinhold Egger. Electron-phonon scattering in topological insulator thin films. *Phys. Rev. B*, 85:035441, Jan 2012.

[36] Lucas Barreto, Lisa Kühnemund, Frederik Edler, Christoph Tegenkamp, Jianli Mi, Martin Bremholm, Bo Brummerstedt Iversen, Christian Frydendahl, Marco Bianchi, and Philip Hofmann. Surface-Dominated Transport on a Bulk Topological Insulator. *Nano Lett.*, 14(7):3755–3760, 2014.

[37] S. K. Mishra, S. Satpathy, and O. Jepsen. Electronic structure and thermoelectric properties of bismuth telluride and bismuth selenide. *J. Phys.: Condens. Matter*, 9(2):461, 1997.

[38] K. Kadel, Latha Kumari, WZ Li, Jian Yu Huang, and Paula P. Provencio. Synthesis and thermoelectric properties of Bi_2Se_3 nanostructures. *Nanoscale Res. Lett.*, 6(1):57, 2010.

[39] H. J. Goldsmid. *Thermoelectric Refrigeration*. Springer, 1964.

[40] X. Zhu, L. Santos, R. Sankar, S. Chikara, C. Howard, F. C. Chou, C. Chamon, and M. El-Batanouny. Interaction of Phonons and Dirac Fermions on the Surface of Bi2Se3 : A Strong Kohn Anomaly. *Phys. Rev. Lett.*, 107:186102–1–5, 2011.

[41] P. D. C. King, R. C. Hatch, M. Bianchi, R. Ovsyannikov, C. Lupulescu, G. Landolt, B. Slomski, J. H. Dil, D. Guan, J. L. Mi, E. D. L. Rienks, J. Fink, A. Lindblad, S. Svensson, S. Bao, G. Balakrishnan, B. B. Iversen, J. Osterwalder, W. Eberhardt, F. Baumberger, and Ph. Hofmann. Large tunable rashba spin splitting of a two-dimensional electron gas in Bi_2Se_3. *Phys. Rev. Lett.*, 107:096802, Aug 2011.

[42] X. Chen, H. D. Zhou, A. Kiswandhi, I. Miotkowski, Y. P. Chen, P. A. Sharma, A. L. Lima Sharma, M. A. Hekmaty, D. Smirnov, and Z. Jiang. Thermal expansion coefficients of Bi_2Se_3 and Sb_2Te_3 crystals from 10 K to 270 K. *Appl. Phys. Lett.*, 99(26):261912, 2011.

[43] G. E. Shoemake, J. A. Rayne, and R. W. Ure. Specific heat of n- and p-type Bi_2Te_3 from 1.4 to 90 K. *Phys. Rev.*, 185:1046–1056, Sep 1969.

[44] F.C.M.J.M. van Delft. Bulk and surface Debye temperatures in relation to cohesive energy and Lennard-Jones potentials. *Surf. Sci.*, 251-252:690–695, July 1991.

[45] H. Shichibe, Y. Satake, K. Watanabe, A. Kinjyo, A. Kunihara, Y. Yamada, M. Sasaki, W. W. Hayes, and J. R. Manson. Probing interlayer interactions between graphene and metal substrates by supersonic rare-gas atom scattering. *Phys. Rev. B*, 91:155403, Apr 2015.

[46] W. Allison, R. F. Willis, and M. Cardillo. Origin of the anomalous low-frequency losses observed in the inelastic scattering of He atoms from LiF(001). *Phys. Rev. B*, 23:6824–6827, Jun 1981.

[47] Bao-Tian Wang and Ping Zhang. Phonon spectrum and bonding properties of Bi_2Se_3: Role of strong spin-orbit interaction. *Appl. Phys. Lett.*, 100(8):082109, 2012.

[48] F.W.de Wette W. Kress. *Surface Phonons*, volume 21. Springer, 1991.

[49] Sébastien Giraud, Arijit Kundu, and Reinhold Egger. Electron-phonon scattering in topological insulator thin films. *Phys. Rev. B*, 85:035441, Jan 2012.

[50] D. Campi. Private communication. 2017.

[51] Paolo Giannozzi, Stefano Baroni, Nicola Bonini, Matteo Calandra, Roberto Car, Carlo Cavazzoni, Davide Ceresoli, Guido L Chiarotti, Matteo Cococcioni, Ismaila Dabo, Andrea Dal Corso, Stefano de Gironcoli, Stefano Fabris, Guido Fratesi, Ralph Gebauer, Uwe Gerstmann, Christos Gougoussis, Anton Kokalj, Michele Lazzeri, Layla Martin-Samos, Nicola Marzari, Francesco Mauri, Riccardo Mazzarello, Stefano Paolini, Alfredo Pasquarello, Lorenzo Paulatto, Carlo Sbraccia, Sandro Scandolo, Gabriele Sclauzero, Ari P Seitsonen, Alexander Smogunov, Paolo Umari, and Renata M Wentzcovitch. Quantum espresso: a modular and open-source software project for quantum simulations of materials. *J. Phys.: Condens. Matter*, 21(39):395502 (19pp), 2009.

[52] M. Alcántara Ortigoza, I. Yu. Sklyadneva, R. Heid, E. V. Chulkov, T. S. Rahman, K.-P. Bohnen, and P. M. Echenique. Ab initio. *Phys. Rev. B*, 90:195438, Nov 2014.

[53] S. Sugai, Y. Takayanagi, and N. Hayamizu. Phason and Amplitudon in the Charge-Density-Wave Phase of One-Dimensional Charge Stripes in $La_{2-x}Sr_xCuO_4$. *Phys. Rev. Lett.*, 96:137003, Apr 2006.

[54] Darius H. Torchinsky, Fahad Mahmood, Anthony T. Bollinger, Ivan Bozovic, and Nuh Gedik. Fluctuating charge-density waves in a cuprate superconductor. *Nat. Mater.*, 12(5):387–391, May 2013.

[55] I. Yu. Sklyadneva, G. Benedek, E. V. Chulkov, P. M. Echenique, R. Heid, K.-P. Bohnen, and J. P. Toennies. Mode-Selected Electron-Phonon Coupling in Superconducting Pb Nanofilms Determined from He Atom Scattering. *Phys. Rev. Lett.*, 107:095502, Aug 2011.

[56] G. Benedek, M. Bernasconi, K.-P. Bohnen, D. Campi, E. V. Chulkov, P. M. Echenique, R. Heid, I. Yu. Sklyadneva, and J. P. Toennies. Unveiling mode-selected

electron-phonon interactions in metal films by helium atom scattering. *Phys. Chem. Chem. Phys.*, 16(16):7159, 2014.

[57] E. M. McIntosh, P. R. Kole, M. El-Batanouny, D. M. Chisnall, J. Ellis, and W. Allison. Measurement of the Phason Dispersion of Misfit Dislocations on the Au(111) Surface. *Phys. Rev. Lett.*, 110:086103, Feb 2013.

[58] U. Harten, A. M. Lahee, J. Peter Toennies, and Ch. Wöll. Observation of a Soliton Reconstruction of Au(111) by High-Resolution Helium-Atom Diffraction. *Phys. Rev. Lett.*, 54:2619–2622, Jun 1985.

[59] D. Maccariello, D. Campi, A. Al Taleb, G. Benedek, D. Farias, M. Bernasconi, and R. Miranda. Low-energy excitations of graphene on Ru(0 0 0 1). *Carbon*, 93:1 – 10, 2015.

[60] Christian R. Ast and Hartmut Höchst. Indication of Charge-Density-Wave Formation in Bi(111). *Phys. Rev. Lett.*, 90:016403, Jan 2003.

[61] T. K. Kim, J. Wells, C. Kirkegaard, Z. Li, S. V. Hoffmann, J. E. Gayone, I. Fernandez-Torrente, P. Häberle, J. I. Pascual, K. T. Moore, A. J. Schwartz, H. He, J. C. H. Spence, K. H. Downing, S. Lazar, F. D. Tichelaar, S. V. Borisenko, M. Knupfer, and Ph. Hofmann. Evidence against a charge density wave on Bi(111). *Phys. Rev. B*, 72:085440, Aug 2005.

[62] K. Sugawara, T. Sato, S. Souma, T. Takahashi, M. Arai, and T. Sasaki. Fermi Surface and Anisotropic Spin-Orbit Coupling of Sb(111) Studied by Angle-Resolved Photoemission Spectroscopy. *Phys. Rev. Lett.*, 96:046411, Feb 2006.

[63] Davide Campi, Marco Bernasconi, and Giorgio Benedek. Phonons and electron-phonon interaction at the Sb(111) surface. *Phys. Rev. B*, 86:075446, Aug 2012.

[64] Anton Tamtögl, Patrick Kraus, Michael Mayrhofer-Reinhartshuber, Giorgio Benedek, and Wolfgang E. Ernst. Surface Phonon Dispersion of Sb(111). in preparation (2017).

[65] E.W. Plummer, Junren Shi, S.-J. Tang, Eli Rotenberg, and S.D. Kevan. Enhanced electron-phonon coupling at metal surfaces. *Prog. Surf. Sci.*, 74(1-8):251 – 268, 2003. Maria Steslicka Memorial Volume.

[66] C. S. Jayanthi, H. Bilz, W. Kress, and G. Benedek. Nature of surface-phonon anomalies in noble metals. *Phys. Rev. Lett.*, 59:795–798, Aug 1987.